Simulation of Chemotactic Migration of a Crawling Cell by Finite Elements in a Two-dimensional Framework

David Hernández-Aristizábal

This page has been intentionally left blank.

Simulación del Movimiento tipo Arrastrado de una Célula en Migración tipo Quimiotáctica por Elementos Finitos en un Dominio Bidimensional

David Hernández Aristizábal

Tesis presentada como requisito parcial para optar al título de:
Magíster en Ingeniería - Ingeniería Mecánica

Director:
Ph.D. Diego Alexander Garzón Alvarado
Codirector:
PhD. Anotida Madzvamuse

Línea de Investigación:
Modelación computacional de sistemas biológicos
Grupo de Investigación:
GNUM

Universidad Nacional de Colombia
Facultad de Ingeniería
Departamentdo de Ingeniería Mecánica y Mecatrónica
Bogotá, Colombia
2021

This page has been intentionally left blank.

Acknowledgements

This page has been intentionally left blank.

Dedication

To Luz Elena.

This page has been intentionally left blank.

Contents

List of Figures

This page has been intentionally left blank.

List of Tables

This page has been intentionally left blank.

Nomenclature

β_1 and β_2 Positive constants that control the evolution of λ

$\boldsymbol{\kappa}$ The mean curvature vector

$\boldsymbol{\kappa}^h$ Quadratic finite element approximation of $\boldsymbol{\kappa}$

$\boldsymbol{\mu}$ The outward conormal unit vector

$\boldsymbol{\sigma}_c$ Contractile stress

$\boldsymbol{\sigma}_p$ Protrusive stress

$\boldsymbol{\sigma}_s$ The stress induced by the irregularity of the elements

$\boldsymbol{\sigma}$ Cauchy stress

$\boldsymbol{\varepsilon}$ The elastic strain

$\boldsymbol{\varphi}$ Test function

$\boldsymbol{\vartheta}$ Test function

$\boldsymbol{\zeta}$ $2 \times 2N^b$ matrix of basis functions

$\boldsymbol{F}_s$ Force induced by the strain produced as a consequence of low mesh quality

$\boldsymbol{H}^1$ $H^1(\Gamma) \times H^1(\Gamma)$

$\boldsymbol{n}$ The outward-pointing unit normal to the surface

$\boldsymbol{T}$ Tension traction on the membrane

$\boldsymbol{u}$ Displacement

$\boldsymbol{U}^\star$ Nodal displacements from irregular triangles to reference regular triangles

$\boldsymbol{u}^h$	Finite element approximation of $\boldsymbol{u}$
$\boldsymbol{x}^h$	Quadratic finite element approximation of $\boldsymbol{x}$
χ	One-dimensional linear basis functions
δ	A factor of proportionality of the rigidity of the membrane
Δ_Γ	The Laplace-Beltrami operator
Γ	Two-dimensional evolving hypersurface representing the cell
γ	Reaction strength on the membrane
Γ^h	Piecewise linear approximation of Γ
Γ^q	Piecewise-quadratic surface
$\hat{a}_1$	The average value of a_1
λ	Area-control variable
$\mathbf{B}$	$2N^b \times 2N^b$ matrix of differentiated basis functions
$\mathbf{K}$	Nodal mean curvature vector
$\mathbf{U}$	Vector of nodal values of the finite element approximation of $\boldsymbol{u}$
$\mathbf{v}$	Material velocity
$\mathcal{D}$	The plane-stress elastic stiffness matrix
$\mathcal{F}$	Reaction vector
$\mathcal{I}$	Three-dimensional identity matrix
$\mathcal{M}$	Mass matrix
$\mathcal{S}$	Stiffness matrix
$\mathfrak{A}_l$	Total arc length of the piecewise quadratic surface
$\mathfrak{A}_l^{z_e}$	The arc length from the first node until the end of element e

$\mathfrak{a}_T$ Area of a triangle

$\mathfrak{p}_T$ Perimeter of a triangle

$\mathscr{Q}_{\min}$ Mesh minimum quality

$\mathscr{Q}_{\min}^{\star}$ Minimum allowed element quality

$\mathscr{Q}_T$ The quality of a triangle

∇_Γ The tangential gradient operator

ν Poisson's ratio

Ω Two-dimensional evolving domain representing the cell

Ω^h Piecewise linear approximation of Ω

$\partial^\bullet$ Material derivative

ϕ Test function

ϕ^h One-dimensional piecewise-linear test function

$^b\mathbf{A}$ Nodal approximation vector of a_b

$^b\mathcal{A}$ Finite element approximation of a_b

$^k\mathbf{A}$ Nodal approximation vector of a_k

$^k\mathcal{A}$ Piecewise linear approximation of a_k

$_e\mathfrak{A}_l$ Arc length of a quadratic surface element

Ψ Elastic constant proportional to the strength of the adhesion

τ Discrete time step

θ One-dimensional quadratic basis functions

ε_0 Factor of and proportionality of the strain induced by the protrusive and contractile forces

φ Test function

φ^h Two-dimensional discrete test function

ζ Basis functions for linear triangular elements

ζ Test function

A Area of Ω

A_0 Initial area of Ω

a_1 Autocatalytic activator on the membrane

a_2 Global inhibitor on the membrane

a_3 Local inhibitor on the membrane

a_b Actin-network variable

C_b The decay rate of a_b

d_1 Diffusion coefficient of a_1

d_3 Diffusion coefficient of a_3

d_b Diffusion coefficient of a_b

dA/dt Rate of change of the area of Ω

E Young's modulus

E^b Number of linear triangular elements

E^q Number of surface quadratic elements (equal to half E^s)

E^s Number of linear surface elements

H^1 Hilbert space

$H_{\boldsymbol{x}}$ The distance from a point $\boldsymbol{x}$ on the membrane to the signalling point

k_1 The basic production of a_1

k_2 The production of a_3

L_e^q Quadratic surface elements

N^b Number of bulk nodes

N^s	Number of surface nodes
N_{GP}	Number of Gaussian points
r_1	The consumption rate of a_1
r_2	The production and consumption rate of a_2
r_3	The consumption rate of a_3
RND	A random number
s_1	The saturation rate of the local catalysis
s_3	The Michaelis-Menten constant
s_e	The signalling parameter which captures chemotactic gradients and noise
T_e	A triangular element

This page has been intentionally left blank.

Chapter 1

Introduction

In this chapter, a general context of the thesis is presented. We shall see a review of the current biological and computational developments regarding cell migrations. Thus, this chapter is divided into the following sections: Section 1.1 where a description of the subject is presented, Section 1.2 where the problem to be solved in this thesis is established, Section 1.3 which includes the objectives leading to the solution of such problem, and Section 1.4 indicates the organisation of the text.

1.1 General Overview

Cell motility is a phenomenon that occurs in every stage of life. From embryonic development (Uriu et al., 2014), to wound healing (Morales, 2007), to immune response (Othmer, 2019), among others, where cells migrate from one place to another. Migration is also part of phenomena of negative impact such as cancer metastasis (Warner et al., 2019). Further, there are also spontaneous movements that do not lead to migration but only to shape changes (Luxenburg and Zaidel-bar, 2019). However, the knowledge about cell motility is still incomplete.

It is known that cell motility as a product of a reaccommodation of the cytoskeleton, specially the actin cytoskeleton. The actin cytoskeleton is composed of a cross-linked array of actin filaments (F-actin), the polymeric form of actin (G-actin), and associated proteins (proteins that interact with both G-actin and F-actin) (Shah and Keren, 2013). This array is mainly located at the cell cortex, beneath the cell membrane. At this region, there exists a constant polymerisation and depolymerisation of F-actin. It also grows in a polarised fashion because one end has greater affinity to G-actin, therefore the growth speed is faster at that end. In contrast, the opposite end depolymerises faster. This asymmetry allows the cytoskeleton to push the membrane in a specific direction forming protrusions (Warner et al., 2019).

The migration process can be accomplished by several mechanisms from swimming to crawling (Othmer, 2019). Nonetheless, Alberts et al. (2015) pointed out that animal cells most of the time move crawling. This mechanism can be divided into: (Alberts et al., 2015) protrusion, attachment and traction. These can occur simultaneously, as in keratocytes, or in a more independent fashion, as in fibroblasts. Protrusion is the process of pushing the membrane to new regions. Attachment

takes place when the cytoskeleton binds to the substratum by adhesion proteins. Finally, traction makes the rear (the not protruding edge) move forwards.

Apart from migration the actin cytoskeleton exhibits travelling waves along the cell cortex too Allard and Mogilner (2013). These waves might be involved in exploration of the environment and avoidance of obstacles. Therefore, it must be at least another complementary mechanism to switch from travelling waves to migration and the other way around. Such mechanism is called cell signalling.

Cells can sense different biomechanical and biochemical stimuli from the outside. The former can be detected by deformation, osmotic shock, shear stress, external forces, extracellular matrix stiffness, among others (Cheng et al., 2017). The later stimuli are mainly chemotactic. Here cells can perceive differences in concentration of some molecules, such as growth factors. These concentration gradients indicate the migration direction, which may be either upward or downward (Chang et al., 2003). Once cells recognised a gradient, several signalling pathways are triggered which yield changes in the cytoskeleton (Warner et al., 2019). Lastly, Shah and Keren (2013) reported that biomechanical phenomena may affect directly the cytoskeleton kinetics. For example, reaction rates can be dependent on the stresses, which further complicates the dynamics.

The knowledge about cell migration has been realised mainly by experimental means. For example, several techniques have been developed for cell tracking (Chang et al., 2003; Jeong et al., 2019; Ojima et al., 2012; Piltti et al., 2018; Vu et al., 2019), force measurement (Ting et al., 2012), protein activity (Jung et al., 2011), among others. However, in the last decades researches have also explored mathematical models, which can be classified as continuous and discrete. The former models describe cells as a continuum medium, i.e., they quantify cell density. Contrarily, the later models describe each cell as a separate entity.

In continuum medium, cell density dynamics is generally represented by equations with reaction, diffusion or convective terms. For example, (Murray, 2002, 2003) described some chemotactic models with reaction-diffusion equations where the cell density rate was dependent on the Laplacian of some attractive agent.

Discrete models can further be classified as: models with extracellular interactions, (ii) models with intracellular interactions, and (iii) models with both extra and intracellular interactions. Harris (2017); Zhao et al. (2017) introduced models with extracellular interactions. Harris (2017) modelled the formation of cell clusters using a diffusive chemotactic signal emitted by each cell. Here, cell where modelled as particles. Zhao et al. (2017) introduced the Dynamic Cellular Finite-element Method (DyCelFEM) which accounts for individual and collective cell migration triggered by chemotaxis. This model includes cell proliferation, chemotaxis and mechanical deformation and was able to simulate wound healing.

Alt and Tranquillo (1995) introduced a model with intracellular interactions. They considered a reaction-convection system to describe the G- and F-actin dynamics and a friction, protrusion, retraction, superficial tension and shear force balance to describe the mechanical behaviour. They obtained autonomous travelling waves in a polar-coordinate framework.

The last group of mathematical models includes (but is not limited to) the works

in (Fuhrmann et al., 2007; Séguis et al., 2012; Stéphanou and Tracqui, 2002). Séguis et al. (2012) introduced a chemotactic model with rigid bodies. They considered substrate forces by applying the Stokes equation assuming low Reynolds' numbers. Stéphanou and Tracqui (2002) extended the model by Alt and Tranquillo (1995) including intercellular interactions, a chemotactic environment and substrate resistance. Fuhrmann et al. (2007) introduced a model that takes the end and direction of actin fillaments as variables. Their model exposed polarisation starting from a not polarised state. Based on their results, they also suggested that the amount of mechanisms able to trigger migration does not affect the occurrence of movement, but does affect its robustness.

The above mentioned models deal with either or both chemical reaction kinetic and mass transport systems and mechanical systems. Allard and Mogilner (2013); Bhattacharya and Iglesias (2016) argued that the chemical reaction kinetics may be modelled as excitable systems. For example, systems with multiple steady states where perturbations might lead to a jump from one steady state to another (Seydel, 2010). This type of response can be appropriate to describe behavioural changes such as polarisation.

Mori et al. (2008) introduced an excitable system to model cell polarisation. It considers the activation and deactivation of a Rho protein in a one-dimensional domain. The model shows the following fundamental properties: (i) it can evolve into a polarised state from a homogeneous state due to external perturbations; (ii) once the external stimulus is gone it conserves the polarisation; however (iii) under the presence of other external stimulus it can change the polarisation orientation; and (iv) by directly perturbing the homogeneous steady state, provided that the perturbation is above some threshold, it can adopt a polarised state. Mori et al. (2008) indicated that the keys of their model are: (i) mass conservation, (ii) difference between the diffusion coefficients and (iii) bistability of the reactive terms. These properties allow the system to develop a travelling wave whose velocity becomes zero within the domain. Camley et al. (2017) extended the model by coupling a biomechanical system in a two-dimensional framework. They found a direct connection between the wave-pinning response and the domain shape. Cusseddu et al. (2019) also extended the model to two and three dimensions and proved that bistability and polarisation also apply in these dimensions.

On the other hand, Goehring and Grill (2013); Meinhardt (1999) suggested that the kinetics may be described by Turing instabilities. In this case, spatial stable patterns evolve in the domain. This mechanism was first explained in (Turing, 1952) and has been widely implemented in biology (Rodrigues et al., 2014). Some examples of systems that can have Turing instabilities are the works presented in (Gierer and Meinhardt, 1972; Schnakenberg, 1979; Sel'kov, 1968) which have also been tested and analysed with heterogeneous parameters as in (Garzón-Alvarado et al., 2012; Page et al., 2003, 2005).

The main advantage of Turing instabilities is the possibility to develop a highly polarised state even from small perturbations. This could account for signalling amplification on the cell membrane, a key stage of cell polarisation. Meinhardt (1999) introduced a model for cell migration able to adapt to external cues and to intensify

such cues. The adaptation is accomplished by a space-dependent parameter which varies according to some external signal and the cue intensification is driven by the Turing instability mechanism. This model has been implemented and coupled to mechanical systems in other works, for example (Campbell et al., 2017; Elliott et al., 2012; Neilson et al., 2011). They all applied the model on evolving hypersurfaces. Neilson et al. (2011) implemented it in a two-dimensional, Campbell et al. (2017) in a three-dimensional and Elliott et al. (2012) in both a two- and a three-dimensional evolving hypersurfaces. In the works (Elliott et al., 2012; Neilson et al., 2011) the authors defined a chemotactic signal with noise and defined normal forces proportional to the concentration of the reactants. In both works the cells exhibited a directional movement with competing protrusions. In (Campbell et al., 2017) a completely noisy signal was used and the cells showed some directional movement. These works then demonstrate the ability of Meinhardt's model to reproduce the required cell polarisation for migration.

However, Meinhardt's model as well as the wave-pinning do not offer a biologically real representation of the dynamics of cell polarisation since their variables are not directly motivated by molecular species (Othmer, 2019). From this point of view works as the presented in (Cheng and Othmer, 2016; Holmes et al., 2017) are more realistic. Cheng and Othmer (2016) introduced a completely biologically motivated model to simulate the polarisation signalling pathway from the activation of the receptors to the activation of RAS proteins. This model was rigorously compared with experimental results and showed great consistency. However, it is much more computationally expensive. For its part, Holmes et al. (2017) proposed two competing proteins, Rac1 and RhoA. The former promoting protrusion and the latter contraction. The model successfully expressed polarisation and adaptation. Nonetheless, it does not include spatial effects and the activation and deactivation of poles are binary.

Regarding the momentum equation, all the above mentioned models but the presented in (Alt and Tranquillo, 1995; Stéphanou and Tracqui, 2002), considered protrusion forces only on the membrane. Alt and Tranquillo (1995); Stéphanou and Tracqui (2002) also considered forces on the membrane but as hydrostatic effects. Since protrusions are consequence of F-actin growth and their adhesion to the substratum, it would be interesting to apply the forces within the cytoskeleton. Further, the membrane tension is often used as a volume (or area) control variable.

Due to the complexity of these models they are generally solved numerically. However, the numerical solution is also nontrivial. The methods have to be able to capture the effects on the evolving variables of a moving domain. Additionally, they also have to deal with mesh quality issues. Further, since cell polarisation first occurs on the membrane, methods able to solve PDEs on evolving surfaces are essential. Finite element theory on solving PDEs on evolving surfaces can be found in (Barrett et al., 2020; Dziuk and Elliott, 2007, 2013). In the seminal work by Dziuk and Elliott (2007) the evolving-surface finite element method (ESFEM) was formulated. From then on, it has been implemented to solve PDEs on evolving surfaces as in (Barreira et al., 2011; Elliott et al., 2012; Elliott and Styles, 2012; Frittelli et al., 2018). Other works have implemented Eulerian approximations, such

as in (Campbell et al., 2017) by means of finite-difference schemes, and arbitrary Lagrangian Eulerian approximations have also been formulated, such as in (Neilson et al., 2011) by using level set methods and the surface finite element method.

Finally, to deal with mesh quality issues there are three techniques: remeshing schemes, smoothing algorithm and adaptive moving mesh methods. The first is based on building a whole new mesh to better discretise the domain when the mesh is too distorted. This method requires meshing techniques, as the reported in (Engwirda, 2005, 2014), and generally a mapping of the variables. Smoothing algorithms refer to improving mesh quality by reorganising the nodes, as the introduced in (Durand et al., 2019). They are usually iterative and required numerical methods able to take into account artificial mesh movement. Finally, adaptive moving mesh methods also improve mesh quality by reorganising the nodes but this reorganisation also includes targeting areas of refinement, see for example (Mackenzie et al., 2019).

1.2   Why this Research

Undoubtedly, cell migration is an ubiquitous in biology. However, the number of factors simultaneously interacting make it complex and difficult to characterise. In addition, setting up in vitro or in vivo experiments is usually expensive and comes with an ethical constrain. It is therefore desired that in the future mathematical models will be able to accurately describe biological phenomena, just as the performance of complete machines can be tested in silico nowadays. Such advance would benefit significantly our understanding of biology and reduce the usage of animals in experiments. In particular, the reduction of animals in experiments is of highly interest to deal with ethical concerns; nowadays many animals are used in experiments in vivo and in vitro, where extraction of their cells is required. Thus, willing to shed light in different cell motility phenomena such as mitosis, cancer metastasis, cell migration, cell proliferation, among others, in this project, a computational tool able to mimic cell motility, for instance, chemotactic cell migration, is constructed. Mathematically, this thesis deals with the following problem: to build a computational tool able to simulate evolving domains where there are biomechanical and biochemical interactions on the surface and in the bulk, hence potentially able to predict cell migration.

1.3   Objectives

1.3.1   General

To simulate and imitate by finite elements the process of cell migration due to chemotaxis of an eukaryotic cell.

1.3.2   Specific

- To formulate a mathematical model coupling the biochemical and biomechanical interactions during cell migration.

- To implement the previous model.

- To verify the biological plausability.

1.4   Thesis Organisation

To address the above objectives, we shall see in Chapter 2 a brief description of the biological theory focusing on the dynamics of the cytoskeleton and the signalling pathways involved in cell migration. In Chapter 3 the mathematical models and the numerical methods are presented as well as the results obtained. Finally, Chapter 4 comprises the conclusions of this dissertation and the future work.

Chapter 2

Biological Description

In this chapter, a brief description of the biological theory is presented. The objective here is to understand the biological phenomena so that they can be properly modelled. As will be seen, the dynamics for cell migration is very complex, therefore it is essential to identify key features to build a simple but still robust mathematical model. This section is organised as follows, in Section 2.1 we shall see the general parts of an eukaryotic cell, namely the membrane, the cytoplasm, and the nucleus, as well as the composition of the cytoskeleton which provides mechanical properties to the cell. Section 2.2 introduces the most relevant components of the actin cytoskeleton and how they interact and lead to protrusion and contraction. In Section 2.3 the signalling pathways that control cell polarisation and therefore the actin dynamics will be described. The interested reader is referred to (Alberts et al., 2015; Lodish et al., 2016; Ridley et al., 2003)

2.1   Basic Aspects

Cells are considered the unit of life. They can constitute a whole organism, e.g. paramecium, or be part of one, e.g. animal cells. The former can be either prokaryotic (less advanced cells as bacteria) or eukaryotic (more advanced cells as animal cells) while the latter can only be eukaryotic. Whereas eukaryotes have clear separated domains, e.g. nucleus and cytoplasm, prokaryotes do not. Although they both show a wide diversity of moving mechanisms, from crawling to swimming to flagellar movement, prokaryotes commonly use flagellar (Jarrell and McBride, 2008) while most eukaryotes prefer crawling (Alberts et al., 2015).

For this exposition let us consider the following domains of a eukaryotic cell: the plasma membrane, the cytoplasm and the nucleus (see Fig. 2.1). The first separates the cell from the environment. It is mainly made up of a lipid bilayer which commonly comprises phospholipids (Alberts et al., 2015). These are molecules with a hydrophobic and a hydrophilic domain, respectively, the tail and the head. The tail consists of two fatty acids while the head is a phosphate group. In each layer, the phosphate groups are in contact with other phosphates and all the tails are pointing in the same direction, then the hyrophobic and hydrophilic domains

are conserved. In the bilayer, the two layers are in contact by their hydrophobic domains. Therefore the phosphate groups are exposed to either the intracellular or the extracellular environment (see box 1 in Fig. 2.1). The plasma membrane also contains other molecules, such as proteins, that allow the interaction between the cell and the environment.
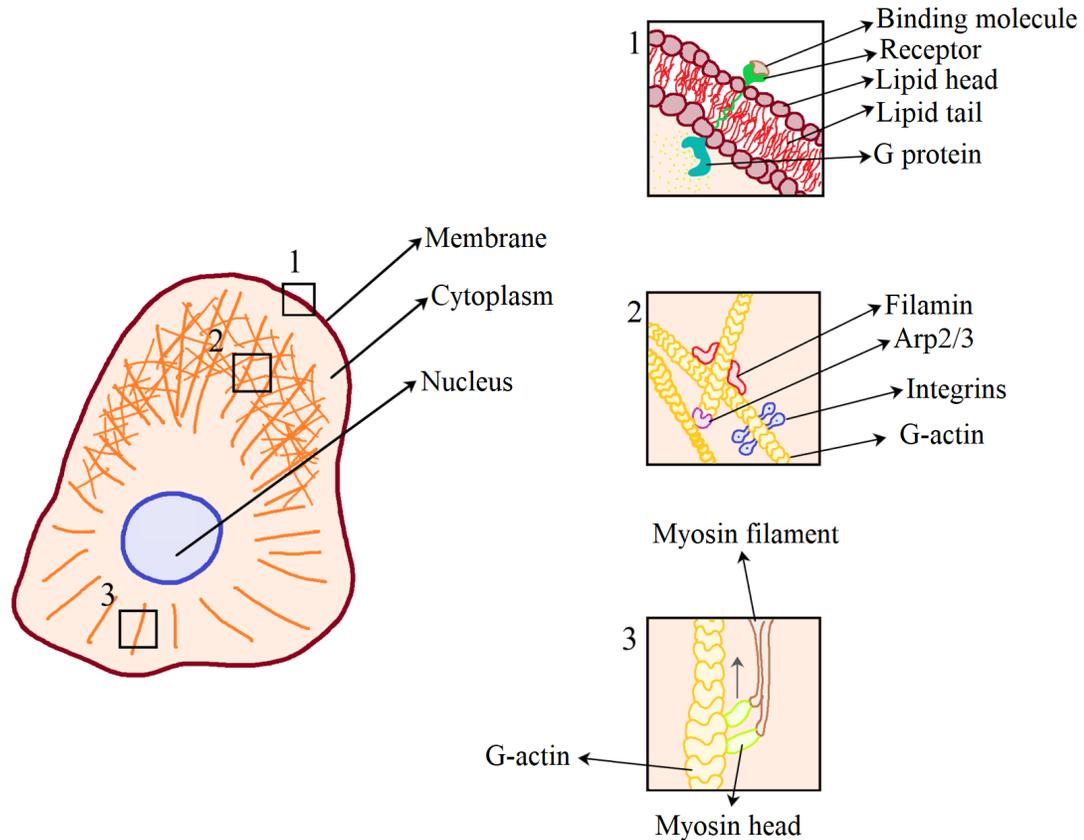
Figure 2.1: Schematic representation of cell domains. Box 1 is a closer look to the plasma membrane, it shows the organisation of the lipid bilayer and some membrane proteins. Box 2 is a closer look to the actin cytoskeleton that illustrates actin network as the interaction of F-actin with some associated proteins that fuel protrusion. In contrast, box 3 is also a closer look to the actin cytoskeleton however here F-actin is interacting with myosin which triggers contractility.

The cytoplasm comprises what is in between the cell membrane and the nuclear envelope (another lipid bilayer that surrounds the nucleus). It then comprises organelles, such as mitochondria, as well as not bounded structures, such as the cytoskeleton (Lodish et al., 2016). In particular, the cytoskeleton provides mechanical properties and topological organisation (Alberts et al., 2015).

The cytoskeleton is mainly composed by three families of molecules: microtubules, intermediate filaments and actin filaments (F-actin). The first control organelle organisation, serve as paths for intracellular transport, and help during cell

division. The second are responsible of mechanical strength. The third regulate shape and locomotion (Alberts et al., 2015). In Fig. 2.1 a schematic representation of the F-actin network is shown. Boxes 2 and 3 show these filaments as the polymerisation of several monomeric actin molecules and their interaction with some associated proteins.

In the figure the upper part (front) of the cell has a denser actin network than the lower part (rear). In migrating cells such polarisation might be a consequence of signalling pathways controlled by the RhoGTPase family of proteins. This organisation of the actin network is what allows cell locomotion. At the front protrusions grow while at the rear the cell contracts.

2.2   Actin Cytoskeleton

The actin cytoskeleton is formed by actin filaments. They have a diameter around 7 nm and can be long up to micrometer scale (Cooper, 2000). Additionally, they interact with each other and several associated proteins to form more complex structures such as webs and bundles (Alberts et al., 2015).

The filaments alone have a constant polymerisation and depolymerisation state at both ends. However, each end has a different affinity to G-actin. The most affine end is known as barbed or plus whereas the other end is called pointed or minus (Lehtimäki et al., 2016). At the barbed end the polymerisation rate of G-actin is higher. Analogously, depolymerisation of F-actin is faster at the pointed end. This asymmetry allows the filaments to move by treadmilling which is the phenomenon of growing at the barbed end and decreasing at the pointed end at almost the same rate that simulates filament translation, as illustrated in Fig. 2.2.

The dynamics of the actin network also includes a wide variety of accessory proteins. They can help to nucleate, form branches, stabilise or destabilise the actin network. In general they modify actin dynamics. See, for example, box 2 in Fig. 2.1. In the figure, three of these proteins are illustrated.

The complex Arp2/3 enhances the nucleation of new filaments as daughters of existing filaments. Alone, it is a very unstable process due to the constant polymerisation and depolymerisation. In fact, many times it fails. Arp2/3 forms at existing filaments and then recruit several actin monomers allowing a rapid elongation of the barbed end (Alberts et al., 2015). Other nucleating proteins, e.g., formins act directly on the barbed end. Proteins like filamins provide cross-linking between filaments which generates stable gel-like webs (Ridley et al., 2003).

Other proteins, like cappings, bind to the ends of the filaments and disable both polymerisation and depolymerisation, i.e. they stabilise the filaments (Lehtimäki et al., 2016). On the other hand, there are also proteins that promote depolymerisation, e.g. coffilins. They are crucial to restock actin monomers that might be needed elsewhere (Lehtimäki et al., 2016). Box 2 in Fig. 2.1 also shows integrins, adhesion clusters that connect the cytoskeleton to the substratum which is crucial to generate protrusive forces. Without anchoring points it would not be possible to create forces, for instance, without them, actin filaments would not be able to push the membrane

Pointed end   Barbed end
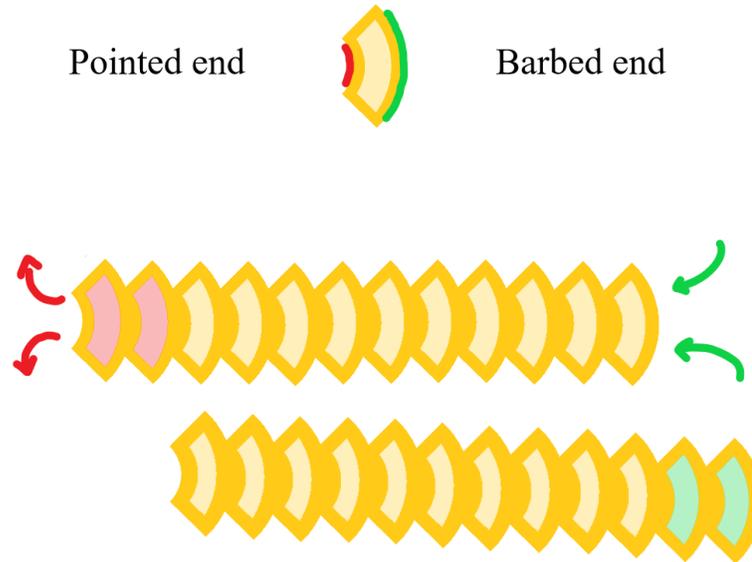
Figure 2.2: Treadmilling scheme. As the filament grows at the barbed end it also
decreases at the pointed end.
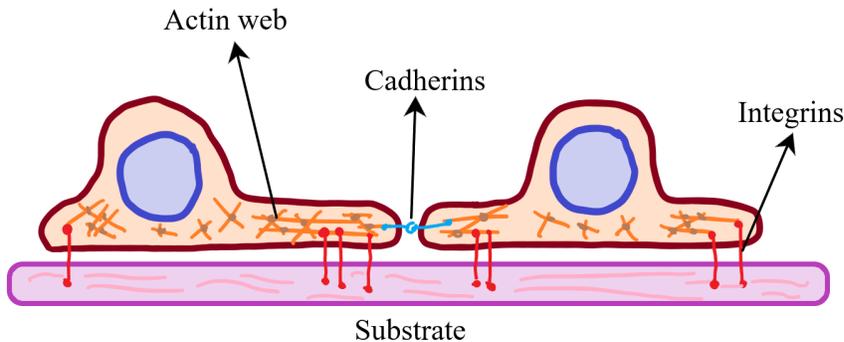
Figure 2.3: Schematic representation of cell-cell and cell-substrate junctions.

as they grow, instead they would be pushed back, a phenomenon called retrograde
flow (Goehring and Grill, 2013). Apart from integrin-mediated junctions there are
also other types of junctions, in particular, cadherin-mediated junctions usually
serve to communicate two cells by binding to each of their cytoskeleton, a schematic
representation of these two type of interactions, cell-substrate and cell-cell junctions
is presented in Fig. 2.3. Box 3 in Fig. 2.1 shows the interaction between F-actin
and myosin proteins. These are motor proteins that can jump from one actin sub-
unit to another (Alberts et al., 2015). Since they are attached to a mother filament
their jumping produces the translation of actin filaments in the opposite direction
of the jump. They are crucial in cell contraction at the rear edge (Lehtimäki et al.,
2016). With such machinery cells are able to modify their cytoskeleton, protrude
and contract in multiple ways.

The protruding structures can be classified by their dimensional nature into:
filopodia, lamellipodia and invadopodia (Alberts et al., 2015). Filopodia are one-
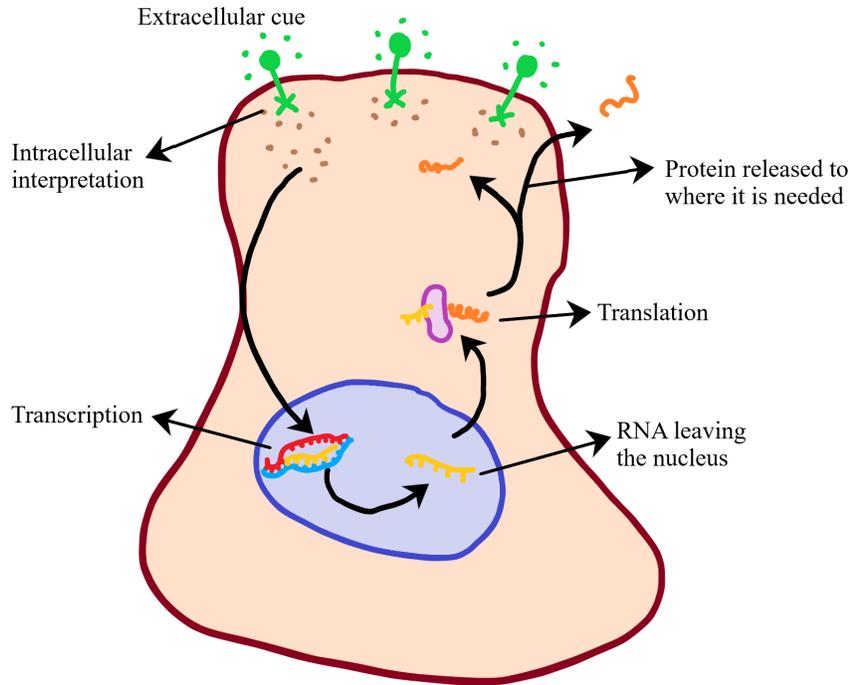
Figure 2.4: Flow of information from extracellular cues to proteins. Cell receptors receive and interpret external cues, downstream transcription takes place in the nucleus, i.e. an RNA chain is form from a DNA strand, latter, such RNA chain leaves the nucleus and reaches a ribosome where it is translated into a protein which may act within the cell or in the extracellular environment.

dimensional structures composed of long and parallel actin-filament bundles, generally 0.1 to 0.3 μm in diameter and up to 10μm long, which serve as sensory organs (Lehtimäki et al., 2016). Lamellipodia are two-dimensional actin-filament-branched networks, 100nm- to 160nm-high sheet-like protrusions, which serve to sense migration cues (Lehtimäki et al., 2016). Lastly, invadopodia, and also posodomes, are three-dimensional structures which can penetrate the extracellular matrix by means of degradation agents (Lehtimäki et al., 2016).

In two-dimensional migration lamellipodia are a key structure. They are formed by a dense branched network of actin filaments with barbed ends pointing towards the plasma membrane. Further, beneath the membrane, the machinery activates growth-driving actin-associated proteins and also deactivates the growth-inhibiting ones (Lehtimäki et al., 2016). We shall take a closer look at the signalling pathways activated in the next section.

2.3 Signalling and Polarisation

Let us begin by understanding how the information flows within and outside the cell. A schematic of that is presented in Fig. 2.4. In general, cells sense external biochemical and biomechanical cues. In directed migration cells usually follow gra-

dients, for example in chemotaxis they follow biochemical gradients and in durotaxis they follow biomehcanical gradients. These external cues trigger a change on the activity of the receptors leading to a downstream activation of the transcription in the nucleus which consists on the formation of an RNA chain from a DNA. The RNA then goes to the cytoplasm and after meeting a ribosome it is translated into amino acids that compose a protein. Finally, the protein goes to where it is required which can be within or outside the cell (Alberts et al., 2015). Although it sounds simple, within the cell there are lots of interconnected signalling networks with both positive and negative loops that make it very complex. Although it sounds simple, within the cell there are lots of interconnected signalling networks with both positive and negative loops that make it very complex, leading to, for example, amplified responses (Ridley et al., 2003).

The ability of cells to sense and amplify a signal allows them to change the cytoskeleton dynamics to protrude and retract in the direction indicated by strong or mild signal. This process translates into movement. In the literature, there are several biological models trying to explain how this machinery works, for example the model described in (Ridley et al., 2003). However, some of the mechanisms involved are not completely understood and vary with cell types. Hence, in this section we will review some particular pathways and proteins associated with cell migration, specially lamellipodium-driven two-dimensional migration.

Let us start with the sensing step. Cells migrate following different types of external stimuli, for example chemical gradients and substrate rigidity (Krause and Gautreau, 2014). The process of responding to chemical gradients is known as chemotaxis and is first activated at the membrane by means of G-protein-coupled receptors (GPCRs) (Cotton and Claing, 2009). The G protein or GTP-binding protein is attached to the plasma membrane and comprises three subunits: α, β and γ. If the protein is inactive the α subunit holds a GDP bound and the three subunits remain toghether. In contrast, when the protien is activated the α subunit exchanges the GDP for a GTP bound and separates from the $\beta - \gamma$ subunits (Alberts et al., 2015). The switch between the inactive and the active states is triggered by the binding of an extracellular molecule to the receptor which changes its form and allows the α subunit to release the GDP bound. Once GPCRs are activated they upregulate guanine nucleotide exchange factors (GEFs) of the RhoGTPase family (RhoGEFs) (Cotton and Claing, 2009).

The RhoGTPase family of proteins is known to control the activity of the actin cytoskeleton (Alberts et al., 2015; Cotton and Claing, 2009; Devreotes and Horwitz, 2015; Ridley, 2015; Ridley et al., 2003; Welf and Haugh, 2011). In particular, RhoA, Rac1 and Cdc42 have received much attention. Rac1 and Cdc42 act on WASP/WAVE-family members which activate nucleation promoting factors (NPFs), such as the Arp2/3 complex, downstream, inducing the branching and growth of the actin-filament network (Steffen et al., 2016). They also downregulate the cofilin activity by acting on p21-activated kinases (PAKs) which in turn phosphorylate LIM kinases (LIMKs) that inhibit cofilins (Devreotes and Horwitz, 2015). Further, WASP/WAVE-family members might also regulate Rac1 and Cdc42 by activating GEFs and GTPase-activating proteins (GAPs) thereupon creating positive and neg-

ative loops (Ridley et al., 2003).

RhoA, in contrast, has an antagonist role with respect to Rac1 and Cdc42. The former is more localised at the rear while the latter is more localised at the front. Additionally, RhoA is highly related to the tail retraction and not very important for membrane protrusion (Salloum et al., 2020). RhoA is involved in Rho/ROCK signalling pathways that promote actomyosin contractility, lamellipodia inhibition and the turnover of focal adhesions (Ridley, 2015). Although RhoA is related to contractility and Rac1 and Cdc42 are related to protrusion, RhoA is involved in protruding pathways at the leading edge (Ridley, 2015) and Rac1 and Cdc42 contributes to contractile pathways at the rear (Devreotes and Horwitz, 2015).

Apart from the RhoGTPase family members, phosphatidylinositol (3, 4, 5) - trisphosphate (PIP3) and phosphatase and tensin homolog (PTEN) activities are also present during cell migration. In fact, they are thought to establish a possible gradient amplifier pathway (Ridley et al., 2003; Welf and Haugh, 2011). In migrating cells, PIP3 rapidly accumulates at the front while PTEN goes to the rear. However, it is neither clear how this occurs nor how their activity affects the cytoskeleton dynamics (Devreotes and Horwitz, 2015). Nonetheless, Ridley et al. (2003) proposed a feedback loop between PIP3 and Rac1: Rac1 activates the phosphoinositide 3-kinases (PI3Ks) at the plasma membrane which in turn upregulates PIP3; then, PIP3 products activate Rac1GEFs which upregulates Rac1. Additionally, PIP3 might also enhance integrin-mediated adhesions at the leading edge which also promotes Rac1 (Ridley et al., 2003).

Last but not least, focal adhesions play an important role, not only because of their mechanical properties but also as signalling intensifiers. At the leading edge, they form a feedback loop with Rac proteins (Ridley, 2015) and regulate myosin II activity by RhoGTPases (Devreotes and Horwitz, 2015). Integrins are the better understood adhesions, they are transmembrane proteins with an α and a β subunits. Each subunit has an extracellular and an intracellular domain which allow the interactions between the extracellular matrix (ECM) and the cytoskeleton. Activation of integrins, by ligands, is then followed by the formation of integrin clusters, establishing a signalling centre connected to the actin dynamics (Calderwood et al., 2013). Finally, they are preferentially activated at the leading edge providing solid traction points (Ridley et al., 2003). As protrusions grow the activity of myosin II increases which promotes their disassembly. In addition, in highly attaching cells, such as fibroblasts, the increased tension at the rear might open calcium channels which in turn might favor the dissasembly (Ridley et al., 2003).

2.4 Key Features

As can be seen, the migration machinery is very complex. However, an initial model can be constructed such that it reproduces the following key features: (i) membrane and cytosolic polarisation (the latter as a downstream effect of the former) and (ii) mechanical response as a result of the actin dynamics. The first feature then encompasses the biochemical dynamics of the actin cytoskeleton while the second

refers to the process of protrusion, attachment and contraction.

Chapter 3

Modelling and Simulation of Cell Migration

3.1   Introduction

Cell migration is an ubiquitous process in life, it can seen at the very beginning, e.g. embryonic development (Uriu et al., 2014), as well as at the very end, e.g. cancer metastasis (Warner et al., 2019). Cells utilise a wide diversity of mechanisms to move, e.g. leukocytes move by pushing their membrane (crawling) and spermatozoa make their flagellum oscillate. Nonetheless, most animal cells particularly prefer crawling (Alberts et al., 2015) which is a three-step process: protrusion, attachment, and traction. Cells need to be constantly modifying their cytoskeleton to be able to accomplish such process. In addition, in many situations, this modification is a response of external cues which trigger different signalling pathways. Thus, cell migration is a complex process involving both biochemical and biomechanical interactions.

Due to that complexity, this phenomenon has attracted engineering and mathematicians willing to shed light on the underlying mechanisms providing consistent models, deep mathematical analysis, and robust numerical methods. The mathematical models require the formulation of biochemical and biomechanical systems. For the former, excitable (Mori et al., 2008) and Turing (Meinhardt, 1999) systems have been proposed, both showing amplification of small cues and ability to reorient after a change of the signal source location. Regarding the latter, most of the previous works have considered viscous and elastic material behaviours within the bulk (Baaijens et al., 2005; George et al., 2013; Preziosi and Tosin, 2009) with tension and bending on the membrane (Campbell et al., 2017; Elliott et al., 2012; Neilson et al., 2011). In addition, this to systems are usually couple by defining a biomechanical term dependent on a biochemical variable as in (Madzvamuse and George, 2013).

In this chapter, we model two-dimensional cell migration which is an idealisation of the real three-dimensional movement; however, in vitro motility is usually consider a two-dimensional phenomenon. We assume that the cell is only composed of its cytoplasm, that it deforms elastically and that, due to the reaccomodation of the

cytoskeleton, no elastic energy is accumulated, as previously done in (Zhao et al., 2017). In addition, we consider membrane tension on the boundary and a thermal-like force leading expansion/contraction driven by the balance between the area change and the state of a biochemical variable. Thus, we take into account the formation of protrusions due to the accumulation of F-actin and the contraction of the cell. Finally, we also assume that the polarisation of the cell is driven by a Turing system and therefore apply the Meinhardt (1999) model for cell polarisation on the membrane and a linear diffusion-depletion system in the cytoplasm to capture the downstream effect of the membrane polarisation.

As a result, we implement a computational framework that mimics the following fundamental migration properties: (i) random and chemotactic membrane polarisation, (ii) downstream polarisation, and (iii) actin-dependent protrusion. For the numerical solution we use finite element methods and Euler schemes, two mesh smoothing techniques and a remeshing algorithm. An extension of de Boor (1973) algorithm is presented to equidistribute the surface mesh, the Durand et al. (2019) method is utilised to smooth the bulk elements, and the remeshing scheme is an application of the toolbox presented in (Engwirda, 2005, 2014).

3.2   Mathematical Model

Let us assume that the cell we want to mimic is moving in a flat surface and that the movement is essentially a two-dimensional, as occurs in in vitro experiments. We can thereupon consider a two-dimensional evolving domain $\Omega(t) \in \mathbb{R}^2 \times [0, T]$ with boundary $\Gamma(t)$ being a two-dimensional evolving hypersurface. Here we will not take into account the nucleus and the whole intracellular environment $\Omega(t)$ will represent the cytoplasm. Obviously, $\Gamma(t)$ will represent the plasma membrane. On $\Gamma(t)$ we will model the signal amplification applying the model of Meinhardt (1999) whose underlying mechanism is Turing instability. Therefore, we assume that the interaction between membrane proteins as GPCR's and a binding molecules as growth factors that leads to polarised states responds to a Turing mechanism. In $\Omega(t)$ we will model the actin-cytoskeleton dynamics by considering a linear diffusion-depletion system. The plasma-membrane dynamics will be independent of the one in the cytoplasm while the boundary conditions for the intracellular system will be proportional to the concentration on the membrane. Thus, instead of directly representing every molecule within the cell, our model mimics the general dynamics on the plasma membrane and within the cell. Finally, we will include elastic deformation as a response of: the actin-cytoskeleton dynamics, the area evolution and the curvature of the plasma membrane.

3.2.1   Plasma-membrane system

First we shall see the mechanism that drives polarisation which initially occurs on the plasma membrane (Cheng and Othmer, 2016). Assuming that Turing instabilities drive polarisation, the Meinhardt (1999) model for cell orientation is an
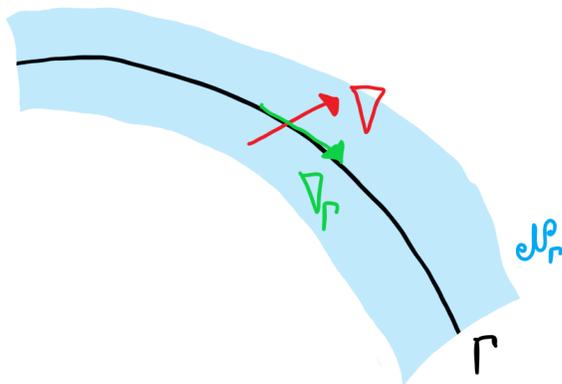
Figure 3.1: Schematic representation of the tangential gradient. Γ is a two-dimensional surface whose neighbourhood is represented by $\mathcal{N}_\Gamma$. The tangential gradient operator ∇_Γ is the projection of the gradient operator ∇ on an extension of Γ.

appropriate choice. This is a reaction-diffusion system with three variables, namely, a_1 (an autocatalytic activator), a_2 (a global inhibitor) and a_3 (a local inhibitor). Although these variables do not represent specific proteins, the response of the system mimics the general interaction of those molecules. Here, we therefore derive the reaction-diffusion equation on an evolving surface and set the mentioned model.

3.2.1.1 Derivation of the reaction-diffusion equation on an evolving surface

Let us start with a given set of $w \in \mathbb{N}$ species a_k, $k = 1, ..., w$ whose dynamics follow a reaction-diffusion behaviour on an evolving surface $\Gamma(t)$. The mass conservation law for the kth species on a portion $\mathcal{R}(t) \subset \Gamma(t)$ then includes the net flux across the boundary $\boldsymbol{q}_k$ and the reaction rates $f_k(\boldsymbol{a})$, $\boldsymbol{a} = [a_1, ..., a_w]^\top$. That is:

$$\frac{\mathrm{d}}{\mathrm{d}t} \int_{\mathcal{R}(t)} a_k = - \int_{\partial\mathcal{R}(t)} \boldsymbol{q}_k \cdot \boldsymbol{\mu} + \int_{\mathcal{R}(t)} f_k(\boldsymbol{a}), \tag{3.1}$$

where $\boldsymbol{\mu}$ is the outward conormal unit vector to $\partial\mathcal{R}(t)$. Following Green's theorem as presented in (Dziuk and Elliott, 2013), the net flux can be rewritten as:

$$- \int_{\partial\mathcal{R}(t)} \boldsymbol{q}_k \cdot \boldsymbol{\mu} = - \int_{\mathcal{R}(t)} \nabla_{\Gamma(t)} \cdot \boldsymbol{q}_k, \tag{3.2}$$

where $\nabla_{\Gamma(t)}$ is the tangential gradient operator. Fig. 3.1 illustrates a schematic representation of this operator which is the projection of the gradient operator on Γ, in other words $\nabla_\Gamma f$ is given by $\nabla\tilde{f} - (\nabla\tilde{f} \cdot \boldsymbol{n})\boldsymbol{n}$ (where $\tilde{f}$ is any differentiable extension of f in $\mathcal{N}_\Gamma$ and $\boldsymbol{n}$ is the unit normal vector to Γ). For further details about the tangential gradient operator see (Barreira et al., 2011; Barrett et al., 2020; Dziuk and Elliott, 2007, 2013; Frittelli et al., 2018). The Reynolds transport

theorem (Dziuk and Elliott, 2007) for a_k is given by:

$$\frac{d}{dt} \int_{\mathcal{R}(t)} a_k = \int_{\mathcal{R}(t)} (\partial^\bullet a_k + a_k \nabla_{\Gamma(t)} \cdot \mathbf{v}), \qquad (3.3)$$

where $\mathbf{v}$ is the material velocity and $\partial^\bullet a_k$ is the material derivative of a_k given by:

$$\partial^\bullet a_k = \frac{\partial a_k}{\partial t} + \mathbf{v} \cdot \nabla_{\Gamma(t)} a_k. \qquad (3.4)$$

Now, replacing Eqs. (3.2) and (3.3) in Eq. (3.1), we obtain:

$$\int_{\mathcal{R}(t)} (\partial^\bullet a_k + a_k \nabla_{\Gamma(t)} \cdot \mathbf{v}) + \int_{\mathcal{R}(t)} \nabla_{\Gamma(t)} \cdot \boldsymbol{q}_k = \int_{\mathcal{R}(t)} f_k(\boldsymbol{a}), \qquad (3.5)$$

and since $\mathcal{R}(t)$ was set arbitrarily, then:

$$\partial^\bullet a_k + a_k \nabla_{\Gamma(t)} \cdot \mathbf{v} + \nabla_{\Gamma(t)} \cdot \boldsymbol{q}_k = f_k(\boldsymbol{a}). \qquad (3.6)$$

Finally, let us assume that the flux across the boundary corresponds to a diffusive flux, thereupon following Fick's law:

$$\boldsymbol{q}_k = -d_k \nabla_{\Gamma(t)} a_k \qquad (3.7)$$

and the reaction-diffusion system on evolving surfaces is given by:

$$\partial^\bullet a_k + a_k \nabla_{\Gamma(t)} \cdot \mathbf{v} - d_k \Delta_{\Gamma(t)} a_k = f_k(\boldsymbol{a}), \qquad (3.8)$$

where $\Delta_{\Gamma(t)}$ is the Laplace-Beltrami operator (which similarly to the tangential gradient accounts for diffusion along the tangential direction), and d_k is the diffusion coefficient of the kth species.

The first term of the left-hand-side of Eq. (3.8) corresponds to the material derivative of the kth species, the second to the dilation due to the growth of the domain, and the third to the diffusion; the term of the right-hand-side represents reaction.

3.2.1.2   Meinhardt model for cell polarisation

Meinhardt (1999) introduced a model able to amplify chemotactic gradients. Starting from an unpolarised state, i.e. a homogeneous state, the model can amplify weak chemotactic gradients. Further, if the chemotactic gradient changes the model is able to reorient. It has been successfully implemented to model chemotactic and random migration in two- and three-dimensional frameworks (Campbell et al., 2017; Elliott et al., 2012; Neilson et al., 2011).

Applying Eq. (3.8) the dimensionless model is:

$$\partial^\bullet a_1 + a_1 \nabla_{\Gamma(t)} \cdot \mathbf{v} - d_1 \Delta_{\Gamma(t)} a_1 = \gamma \left(\frac{s_e \left(\frac{a_1^2}{a_2} + k_1 \right)}{(s_3 + a_3)(1 + s_1 a_1^2)} - r_1 a_1 \right),$$

$$\text{on } \Gamma(t), \qquad (3.9)$$

$$\frac{da_2}{dt} = \gamma \left(r_2 \hat{a}_1 - r_2 a_2 \right), \text{ on } \Gamma(t),$$

$$\partial^\bullet a_3 + a_3 \nabla_{\Gamma(t)} \cdot \mathbf{v} - d_3 \Delta_{\Gamma(t)} a_3 = \gamma \left(k_2 a_1 - r_3 a_3 \right), \text{ on } \Gamma(t),$$

for $t \in [0, T]$. In Eq. (3.9) $\hat{a}_1$ is the average value of a_1; d_1 and d_3 are diffusion coefficients; γ is the strength of the reaction; k_1 is the basic production of the activator and k_2 is the production rate of the local inhibitor; s_1 is the saturation rate of the local catalysis and s_3 is the Michaelis-Menten constant; r_1, r_2 and r_3 are respectively the consumption rate of the activator, the production and consumption rate of the global inhibitor and the consumption rate of the local inhibitor; and s_e is the signalling parameter which captures chemotactic gradients and noise, therefore space-dependent (Meinhardt, 1999). Here we define it as:

$$s_e = r_1 \left(1 + \eta_s \frac{|\Gamma(t)|}{H_{\boldsymbol{x}}^2(\boldsymbol{x})} \right) (1 + \eta_n RND), \tag{3.10}$$

where η_s and η_n are respectively the strength of a signal coming from a specific point outside the cell and the random noise; $|\Gamma(t)|$ is the size of the membrane at time t; $H_{\boldsymbol{x}}$ is the distance from a point $\boldsymbol{x}$ on the membrane to the signalling point; and RND refers to a random number.

3.2.2 Actin-cytoskeleton activity

The polarisation on the membrane leads to the activation of downstream signalling pathways that trigger the reorganisation of the cytoskeleton and thus cytoplasm polarisation. Although we will not address directly any of such signalling pathways, we will take into account the polarisation effect by assuming diffusion of a cytoplasmic chemical whose concentration at the boundary is proportional to the concentration of membrane species and a rate of degradation proportional to its concentration. Thus, for the actin-network dynamics let us consider a linear diffusion-depletion model with Dirichlet boundary conditions dependent on the activity on the membrane. Let a_b be a bulk variable representing the actin-network, then following the formulation of reaction-diffusion equations in moving domains presented in (Madzvamuse et al., 2005), the boundary value problem is given by:

$$\frac{\partial a_b}{\partial t} + \nabla \cdot (\mathbf{v} a_b) = d_b \Delta a_b - C_b a_b \text{ in } \Omega(t), \tag{3.11}$$

$$a_b = a_3 \text{ on } \Gamma(t), \tag{3.12}$$

where d_b and C_b are respectively the diffusion coefficient and the decay rate of a_b. We chose a_3 as the boundary condition instead of a_1 since its profile is smoother and instead of a_2 since a_2 is space-independent.

3.2.3 The mechanical model

We consider that protrusions are triggered by the concentration of the cytoplasmic chemical that mimics cytoplasmic polarisation and that the cell is homogeneously attached to tho substratum. In addition, we take into account membrane tension and contraction due to area change. Therefore the mechanical model regards two type of forces: bulk and surface. The bulk forces represent the protrusive

and contractile effects of actin and myosin while the surface forces represent the membrane tension. Hence, the momentum equation can be given by:

$$\nabla \cdot (\boldsymbol{\sigma}(\nabla \boldsymbol{u}) - \boldsymbol{\sigma_p}(a_b) + \boldsymbol{\sigma_c}(\lambda)) = \Psi \boldsymbol{u}, \text{ in } \Omega(t), \tag{3.13}$$

$$(\boldsymbol{\sigma}(\nabla \boldsymbol{u}) - \boldsymbol{\sigma_p}(a_b) + \boldsymbol{\sigma_c}(\lambda)) \cdot \boldsymbol{n} = \boldsymbol{T} \text{ on } \Gamma(t), \tag{3.14}$$

where $\boldsymbol{\sigma}$, $\boldsymbol{\sigma_p}$ and $\boldsymbol{\sigma_c}$ are respectively the true, the protrusive and the contractile stress tensors, Ψ is an elastic constant proportional to the strength of the adhesion (Zhao et al., 2017), $\boldsymbol{T}$ is the tension traction on the membrane, $\boldsymbol{n}$ is the outward-pointing unit normal to the surface, and λ is an area-control variable which increases if domain grows and decreases if it shrinks allowing to maintain the area.   The tension traction can be computed as proportional to the mean curvature vector $\boldsymbol{\kappa}$ (Elliott et al., 2012; Neilson et al., 2011), which is given by:

$$\boldsymbol{\kappa} = -\Delta_\Gamma \boldsymbol{x}, \tag{3.15}$$

Let us now assume that the deformation process follows an elastic behaviour. This means that the stresses are given by the generalised Hooke's law. By further assuming a plane stress model, the stresses in Eqs. (3.13) and (3.14) are given by:

$$\boldsymbol{\sigma} = \begin{bmatrix} \sigma_{11} \\ \sigma_{22} \\ \sigma_{12} \end{bmatrix} = \mathcal{D}\boldsymbol{\varepsilon} = \frac{E}{1-\nu^2} \begin{bmatrix} 1 & \nu & 0 \\ \nu & 1 & 0 \\ 0 & 0 & \frac{1-\nu}{2} \end{bmatrix} \begin{bmatrix} \varepsilon_{11} \\ \varepsilon_{22} \\ 2\varepsilon_{12} \end{bmatrix}, \tag{3.16}$$

with:

$$\begin{bmatrix} \varepsilon_{11} \\ \varepsilon_{22} \\ 2\varepsilon_{12} \end{bmatrix} = \begin{bmatrix} \dfrac{\partial u_1}{\partial y_1} \\ \dfrac{\partial u_2}{\partial y_2} \\ \dfrac{\partial u_2}{\partial y_1} + \dfrac{\partial u_1}{\partial y_2} \end{bmatrix}, \tag{3.17}$$

$$\boldsymbol{\sigma_p} = a_b \mathcal{D} \begin{bmatrix} \varepsilon_0 \\ \varepsilon_0 \\ 0 \end{bmatrix}, \tag{3.18}$$

$$\boldsymbol{\sigma_c} = \lambda \mathcal{D} \begin{bmatrix} \varepsilon_0 \\ \varepsilon_0 \\ 0 \end{bmatrix}, \tag{3.19}$$

where E and ν are respectively the Young's modulus and the Poisson's ratio, $\mathcal{D}$ is the plane-stress elastic stiffness matrix, $\boldsymbol{\varepsilon}$ is the elastic strain, ε_0 is a factor of proportionality of the strain induced by the protrusive and contractile forces. The area-control variable can be given by (Neilson et al., 2011):

$$\frac{d\lambda}{dt} = \frac{\beta_1 \lambda (A - A_0 + dA/dt)}{A_0(\lambda + \beta_1)} - \beta_2 \lambda, \tag{3.20}$$

$$\lambda(t=0) = \lambda_0,$$

here A, A_0 and dA/dt are respectively the area, the initial area, and the time derivative of the area, and β_1 and β_2 are positive parameters. Following Neilson et al. (2011) we can use λ to define $\boldsymbol{T}$, that is:

$$\boldsymbol{T} = \lambda\delta\boldsymbol{\kappa}, \tag{3.21}$$

δ is a factor of proportionality of the rigidity of the membrane,

As can be seen, Eq. (3.13) is a static equation. In this case, we may consider that after each computation of the biochemical model the system undergoes an elastic deformation. We may also consider that after each deformation the cell rapidly relaxes and no elastic energy is accumulated. That is equivalent to solve Eq. (3.13) without taking into account the pre-strain given by the previous deformation step. This is similar to the work by (Zhao et al., 2017).

Thus, our model is composed of the following differential equations: Eqs. (3.9), (3.11) to (3.15) and (3.20) which describe the evolution of a_1, a_2, a_3, a_b, $\boldsymbol{u}$, $\boldsymbol{\kappa}$ and λ. It is summarised in Table 3.1.

3.3 Numerical Model

Since we have a bulk-surface system of partial differential equations in an evolving domain we need a numerical method able to accurately compute the variables. Several approaches have been implemented. For example in (Novak et al., 2007) finite volumes were applied in a framework with diffusion in the bulk and on the boundary; in (Rätz, 2015; Rätz and Röger, 2014) a phase-field finite-element approach was implemented to deal with a bulk-surface reaction-diffusion system; in (Elliott et al., 2017) a model for the dynamics between membrane receptors and ligands was approximated by the piecewise linear coupled bulk-surface finite element method developed in (Elliott and Ranner, 2013); in (Alhazmi, 2019) the finite element approach is also implemented to solve reaction-diffusion able to form patterns; and in (Frittelli et al., 2021) by combining the virtual element method (Brezzi et al., 2014) and the surface finite element method (Dziuk and Elliott, 2013), the authors delivered a new method to solve bulk-surface PDEs.

In this work we will use the Evolving Surface Finite Element Merhod (ESFEM) (Dziuk and Elliott, 2007) to solve the dynamics on the surface (plasma-membrane). It applies the Reynolds transport theorem to material derivatives to deliver a weak formulation and as a result the velocity and mean curvature of the of the surface are implicit (Dziuk and Elliott, 2013). Applications of this method can be found in (Barreira et al., 2011; Elliott and Styles, 2012; Frittelli et al., 2018). Regarding the bulk, we will further simplify Eq. (3.11) to a time-independent system and since the coupling is through Dirichlet conditions we will use the standard finite element formulation. The remaining time-dependent terms will be solve with backward and forward Euler schemes.

Further, since our model considers an evolving domain, we will also apply smoothing algorithms on the surface and the bulk, as well as a remeshing scheme in case

Name	Equation	Domain
Membrane polarisation	$\partial^\bullet a_1 + a_1 \nabla_{\Gamma(t)} \cdot \mathbf{v} - d_1 \Delta_{\Gamma(t)} a_1 =$ $$\gamma \left(\frac{s_e \left(\frac{a_1^2}{a_2} + k_1 \right)}{(s_3 + a_3)(1 + s_1 a_1^2)} - r_1 a_1 \right)$$	$\boldsymbol{x}(t) \in \Gamma(t)$
	$a_1 = a_{10}$	$\boldsymbol{x}(t) \in \Gamma(0)$
	$\dfrac{da_2}{dt} = \gamma \left(r_2 \hat{a}_1 - r_2 a_2 \right)$	$t \in [0, T]$
	$a_2 = a_{20}$	$t = 0$
	$\partial^\bullet a_3 + a_3 \nabla_{\Gamma(t)} \cdot \mathbf{v} - d_3 \Delta_{\Gamma(t)} a_3 = \gamma \left(k_2 a_1 - r_3 a_3 \right)$	$\boldsymbol{x}(t) \in \Gamma(t)$
	$a_3 = a_{30}$	$\boldsymbol{x}(t) \in \Gamma(0)$
Cytoplasmic polarisation	$\dfrac{\partial a_b}{\partial t} + \nabla \cdot (\mathbf{v} a_b) = d_b \Delta a_b - C_b a_b$	$\boldsymbol{x}(t) \in \Omega(t)$
	$a_b = a_3$	$\boldsymbol{x}(t) \in \Gamma(t)$
	$a_b = a_{b0}$	$\boldsymbol{x}(t) \in \Omega(0)$
Mechanical model	$\nabla \cdot (\boldsymbol{\sigma}(\boldsymbol{u}) - \boldsymbol{\sigma_p}(a_b) + \boldsymbol{\sigma_c}(\lambda)) = \Psi \boldsymbol{u}$	$\boldsymbol{x}(t) \in \Omega(t)$
	$(\boldsymbol{\sigma} - \boldsymbol{\sigma_p} + \boldsymbol{\sigma_c}) \cdot \boldsymbol{n} = \lambda \delta \boldsymbol{\kappa}$	$\boldsymbol{x}(t) \in \Gamma(t)$
	$\boldsymbol{\kappa} = -\Delta_\Gamma \boldsymbol{x}$	$\boldsymbol{x}(t) \in \Gamma(t)$
	$\dfrac{d\lambda}{dt} = \dfrac{\beta_1 \lambda (A - A_0 + dA/dt)}{A_0(\lambda + \beta_1)} - \beta_2 \lambda$	$t \in [0, T]$

Table 3.1: Mathematical model

the former do not work. A schematic representation of our numerical solution is given in Fig. 3.2.

3.3.1 The evolving surface finite element method (ESFEM)

Following (Barreira et al., 2011; Dziuk and Elliott, 2007, 2013; Frittelli et al., 2018) (and as presented in Appendix A.1), the formulation for the standard equation Eq. (3.8) is given by:

$$\frac{\mathrm{d}}{\mathrm{d}t} \left(\mathcal{M}_{ij}(t)^k A_j(t) \right) + d_k \mathcal{S}_{ij}(t)^k A_j(t) = {}^k\mathcal{F}_i(t), \tag{3.22}$$

where $\mathcal{M}$ is the mass matrix given by:

$$\mathcal{M}_{ij}(t) = \int_{\Gamma^h(t)} \chi_i \chi_j,$$

the stiffness matrix $\mathcal{S}$ is:

$$\mathcal{S}_{ij}(t) = \int_{\Gamma^h(t)} \nabla_{\Gamma^h(t)} \chi_i \cdot \nabla_{\Gamma^h(t)} \chi_j,$$

the reaction vector ${}^k\mathcal{F}$:

$$ {}^k\mathcal{F}_i(t) = \int_{\Gamma^h(t)} \chi_i f_k,$$

and ${}^k A$ is the vector of the nodal values of the kth species; $\Gamma^h(t)$ is the piecewise linear approximation of the surface at time t, and χ_i are the basis functions of the linear finite element space $V^h(\Gamma^h(t))$. As can be seen in Eq. (3.22) the ESFEM does not explicitly deals with neither the velocity nor the mean curvature.

We can now derive the fully-implicit system. Applying the Backward-Euler scheme for time integration Eq. (3.22) becomes:

$$\frac{1}{\tau} \left(\mathcal{M}_{ij}{}^{n+1} {}^k A_j{}^{n+1} - \mathcal{M}_{ij}{}^n {}^k A_j{}^n \right) + d_k \mathcal{S}_{ij}{}^{n+1} {}^k A_j{}^{n+1} = {}^k\mathcal{F}_i{}^{n+1}, \tag{3.23}$$

where τ is the discrete time step, the superscripts $(\cdot)^{n+1}$ and $(\cdot)^n$ refer to the solution at time $(n+1)\tau$ and the solution at time $n\tau$, respectively.

The right-hand-side of Eq. (3.23) is in general nonlinear, as in the Meinhardt model for cell polarisation.

3.3.2 Approximation of the global inhibitor

To solve the evolution of a_2 in Eq. (3.9) let us use the Forward-Euler scheme:

$$a_2^{n+1} = \frac{a_2^n + \gamma\tau r_2 \hat{a}_1^n}{1 + \gamma\tau r_2} \tag{3.24}$$

Start

Solve the space-dependent variables of Eq. (3.9) by means of the ESFEM

Solve the space-independent variable of Eq. (3.9) using a Forward-Euler scheme

Solve the bulk biochemical variable in Eqs. (3.11) and (3.12) using a linear finite element method.

Find and apply the displacements solving Eqs. (3.13) and (3.14) implementing a linear finte element method.

Is the simulation done?

Yes → End

No

Equidistribute the surface mesh by de Boor (1973)'s algorithm

Smooth the bulk mesh with Durand et al. (2019)'s scheme

Is the mesh quality good?

Yes → Go to

No

Remesh the domain using the toolbox in (Engwirda, 2005, 2014)

Go to

Figure 3.2: Schematic representation of the numerical solution.

3.3.3   Finite element method in the bulk

Although a finite element to approximate Eqs. (3.11) and (3.12) is presented in (Madzvamuse et al., 2005) we shall make a further simplification of the model to reduce the computational cost. Instead of solving Eqs. (3.11) and (3.12) we will solve a steady state system after every step of the previous method. Therefore, the actin-cytoskeleton activity is now given by:

$$0 = d_b \Delta a_b - C_b a_b \text{ in } \Omega, \tag{3.25}$$

$$a_b = a_1 \text{ on } \Gamma. \tag{3.26}$$

The finite element formulation is straightforward (presented in Appendix A.2) and the problem reads: find $^b\mathbf{A} \in \mathbb{R}^{N^b}$ such that:

$$0 = \int_{\Gamma^h} \left(\zeta_j \nabla \zeta_i\, ^bA_i \right) - d_b \int_{\Omega^h} \left(\nabla \zeta_j \nabla \zeta_i\, ^bA_i \right) - \int_{\Omega^h} \left(\zeta_j C_b\, ^bA_i \right), \tag{3.27}$$

where ζs are the basis functions of the finite element space, in this case we use triangular linear elements, $^b\mathbf{A}$ is the vector of approximated nodal values of a_b, and Ω^h is a triangulation of Ω. Finally, since we know ^bA_i on the surface, from Eq. (3.26), the first term of the right-hand-side is known.

3.3.4   Finite element approximation of the mean curvature vector

It is known that the finite element approximation of the mean curvature vector needs at least quadratic basis functions in order to be convergent (Heine, 2004). Hence, after considering the quadratic finite element space $Q^h := \text{span}\{\theta_j\}_{j=1}^{N^s}$ where $\theta_j(\mathbf{x}_i) = \delta_{ij}$ and $\theta_j|_{L_e^q}$ is either zero or quadratic, let us define $\boldsymbol{Q}^h := Q^h \times Q^h$. Therefore, the finite element problem reads: find $\boldsymbol{\kappa}^h \in \boldsymbol{Q}^h$ such that:

$$\int_{\Gamma^q} \boldsymbol{\vartheta}^h \cdot \boldsymbol{\kappa}^h = \int_{\Gamma^q} \nabla_{\Gamma^q} \boldsymbol{\vartheta}^h \cdot \nabla_{\Gamma^q} \boldsymbol{x}^h \qquad \forall \boldsymbol{\vartheta}^h \in \boldsymbol{Q}^h, \tag{3.28}$$

where $\boldsymbol{\kappa}^h$ and $\boldsymbol{\vartheta}^h$ are the trial and test functions, as shown in Appendix A.3.

3.3.5   Finite element approximation of the mechanical model

The standard finite element method for the mechanical model yields the following algebraic problem (with more detail in Appendix A.4): find $\mathbf{U} \in \mathbb{R}^{2N^b}$ such that

$$\int_\Gamma \boldsymbol{\zeta}^\top \lambda \mathbf{K} - \int_\Omega \mathbf{B}^\top \mathcal{D} \mathbf{B} \mathbf{U} - \int_\Omega (\boldsymbol{F_p} - \boldsymbol{F_c}) - \int_\Omega \boldsymbol{\zeta}^\top \Psi \mathbf{U} = 0, \tag{3.29}$$

where $\mathbf{U}$ and $\mathbf{K}$ are nodal displacement and mean curvature vectors, respectively; $\boldsymbol{\zeta}$ and $\mathbf{B}$ are a matrix of basis functions and a matrix of their derivatives, respectively;

and the force terms are given by:

$$\boldsymbol{F_p} = \mathbf{B}^{\top} a_b \mathcal{D} \begin{bmatrix} 1 \\ 1 \\ 0 \end{bmatrix}, \tag{3.30}$$

$$\boldsymbol{F_c} = \mathbf{B}^{\top} \lambda \mathcal{D} \begin{bmatrix} 1 \\ 1 \\ 0 \end{bmatrix}. \tag{3.31}$$

$$\tag{3.32}$$

3.3.6   Approximation of λ

To finish we need to solve Eq. (3.20). To do this let us use the forward Euler scheme, thus:

$$\frac{d\lambda}{dt} \approx \frac{\lambda^{n+1} - \lambda^m}{\Delta t} = \frac{\beta_1 \lambda (\mathfrak{a}^n - \mathfrak{a}_0 + (\Delta \mathfrak{a}/\Delta t)^n)}{\mathfrak{a}_0 (\lambda^n + \beta_1)} - \beta \lambda^n, \tag{3.33}$$

where the superscripts n and $n+1$ indicate two consecutive steps of deformation, Δt can be regarded as a sensitive parameter to control the change of λ after each deformation, we will set it equal to τ, and $(\Delta \mathfrak{a}/\Delta t)^n$ and $\mathfrak{a}^n$ are respectively the change of area and the area at the n deformation step. Therefore, $(\Delta \mathfrak{a})^n = \mathfrak{a}^n - \mathfrak{a}^{n-1}$.

3.3.7   Mesh Smoothing Algorithms

Two mesh smoothing algorithms are used to improve the quality of the elements throughout the simulation. First a surface mesh equidistribution scheme is implemented by means of the De Boor's algorithm (de Boor, 1973) and the parametric quadratic mesh. Second, the Durand et al. (2019)'s algorithm is implemented to smooth the bulk mesh. Additionally, a remeshing scheme is also utilised in case this algorithm does not improve the mesh quality above a specific threshold. This scheme is based on the Mesh2D toolbox (Engwirda, 2005, 2014). A full presentation of the smoothing algorithms is given in Appendix A.5

3.3.8   The algorithm

1. Set the mesh

    (a) Generate an initial piecewise linear mesh on the surface with a even number of nodes.

    (b) Use the Engwirda (2005, 2014)'s toolbox Mesh 2D to create a piecewise linear triangular mesh.

    (c) Create a quadratic set of surface elements using the same nodes of Item 1a.

    (d) Use the Durand et al. (2019)'s algorithm to smooth the mesh.

2. Solution of field variables at time $n\tau$.

    (a) Approximate a_1 and a_3 through Eq. (3.23).

    (b) Approximate a_2 through Eq. (3.24).

    (c) Approximate a_b, $\boldsymbol{u}$ and $\boldsymbol{\kappa}$ through Eqs. (3.27), (3.29) and (A.29).

    (d) Approximate λ through Eq. (3.33)

    (e) If $n\tau = T$ go to Item 4

3. Improve mesh quality

    (a) Use the de Boor (1973)'s algorithm to equidistribute the the surface mesh.

    (b) Use the Durand et al. (2019)'s to smooth the solid mesh until the mesh change by L_2-norm is less than Ite_{tol} or the maximum number of iterations Ite_{max} is reached. If $\mathscr{Q}_{\text{min}} > \mathscr{Q}_{\text{min}}^\star$ go to Item 2 if not go to Item 1.

4. Finish.

3.4   Numerical Tests

First, we will see the response of the Meinhardt's model on a stationary two-dimensional closed hypersurface. The idea here is to test the response with several combinations of parameters in terms of signal amplification and adaptation to new signals. Second, we will see the results of the whole model under two different combinations of parameters. One of them corresponding to chemotactic migration and the other to completely autonomous movement.

3.4.1   The Meinhardt's model for cell polarisation

Let us fix a_{10}, a_{20}, a_{30} γ, k_2, s_3, r_1, r_2, r_3, η_s and η_n (see Table 3.2) and vary k_2, s_1, d_1 and d_3 (see Table 3.4). For this experiment the domain is a circle of radius 1 centred at $(0,0)$, the finite element discretisation is composed of 2000 nodes and elements and the time step is 0.001. The signal is set at $(5,5)$ from time 0 to 15 and at $(-5,-5)$ from 15 to the end of the simulation.

3.4.2   Chemotactic cell migration

For the solution of the complete model, following Section 3.3.8, let us set the parameters of the biomechanical model presented in Table 3.3. For chemotactic cell migration the parameters of experiment 8 are chosen, as explained in the next section, and the initial domain is bounded by a circle of radius 1 centred at $(0,0)$. Further, the system is tested under an initial signalling point at $(5,5)$ which is then changed at $t = 76$ to $(0,10)$. For this simulation $\tau = 0.001$, the surface was discretised with 2000 equidistant nodes and the size of the bulk mesh was constraint to 0.025.

Parameter	Value
γ	2500
$k_1^\star$	0.1
$s_3^\star$	0.2
$r_1^\star$	0.02
$r_2^\star$	0.03
$r_3^\star$	0.013
$\eta_s^\star$	0.02
$\eta_n^\star$	0.01
a_{10}	1.0
a_{20}	1.0
a_{30}	1.0

Table 3.2: Fixed parameters for the Meinhardt's model of cell polarisation. * indicates values taken from (Meinhardt, 1999).

Parameter	Value
Ψ	0.1
ν	0.45
E	1
δ	0.001
β_1	0.2
β_2	0.001
λ_0	2.0
$\mathscr{Q}_{\min}^\star$	0.55
$Ite_{\max}$	10
Ite_{tol}	0.001
ε_0	0.000025

Table 3.3: Parameters of the biomechanical model

3.4.3   Spontaneous cell movement

In this case, the biomechanical model is implemented with the same parameters presented in Table 3.3, the initial domain is also bounded by a circle of radius 1 centred at $(0, 0)$ and the Meinhardt kinetics is determined by the parameters of the experiment 17, again, this latter choice is explained in the next section. We shall then see unsteady and completely spontaneous movement using those parameters and letting $\eta_s = 0$ and $\eta_n = 0$. The initial mesh and the time step are the same as in the chemotactic migration test.

Experiment	k_2	s_1	d_1	d_3	N_p	w	$a_1^{\max}$	Adaptation
1	0.005	0.005	10	60	1	2.218	6.91	Yes
2	0.005	0.005	10	30	1	2.441	5.69	Yes
3	0.005	0.005	10	20	1	2.677	4.94	Yes
4	0.005	0.005	10	100	1	2.127	7.72	Yes
5	0.005	0.005	10	50	1	2.259	6.6	Yes
6	0.005	0.005	10	15	1	2.934	4.4	Yes
7	0.0025	0.005	10	30	1	2.975	8.1	Yes
8	0.0025	0.005	10	20	1	3.299	7.18	Yes
9	0.0025	0.005	10	15	1	3.654	6.49	Yes
10	0.005	0.0025	10	30	1	2.262	6.48	Yes
11	0.005	0.0025	10	20	1	2.466	5.58	Yes
12	0.005	0.0025	10	15	1	2.680	4.96	Yes
13	0.005	0.01	10	30	1	2.717	4.78	Yes
14	0.005	0.01	10	20	1	3.135	4.15	Yes
15	0.005	0.01	10	15	1	3.415	3.68	Yes
16	0.005	0.005	1	2.5	2	1.949	6.46	No
17	0.005	0.005	1	2	2	2.079	5.94	No

Table 3.4: Summery of the response of the Meinhardt's model for cell polarisation with different parameters.

3.5 Results

3.5.1 The Meinhardt's model for cell polarisation

We can consider the following measures: the number of peaks N_p, the highest value of the activator $a_1^{\max}$, the width w of the peaks above $a_1^{\max}/2$ and whether the model is able to adapt to a new signal. Table 3.4 shows the results of our experiments.

We can see that the experiments 16 and 17, which had $d_1 = 1$ and $d_2 = 2, 2.5$, had a very different response compared to the others. The system developed two coexisting peaks and was not able to adapt to changes in the signal whereas in the other experiments the system developed one peak and was able to reorient. In experiments 1 to 15 $d_1 = 1$ and d_3 varied from 15 to 100. Increasing d_3 made $a_1^{\max}$ larger, however, w decreased and the system was slower to move from one polarised state to another. A reduction in k_2 from 0.005 to 0.0025 provided higher $a_1^{\max}$ and w and decreased the time from one polarised state to another but a further reduction, to for example 0.00125, almost homogenised the response. Finally, in our experiments dropping the value of s_1 increased $a_1^{\max}$ and decreased w.

From these results, the values of the experiment 8 are used in the complete model because it is the combination of parameters that better balances high values $a_1^{\max}$ and w and an adaptation time. Fig. 3.3 shows the results of the simulation with such parameters. The system took around $t = 1.1$ to reach a stable polarised state.
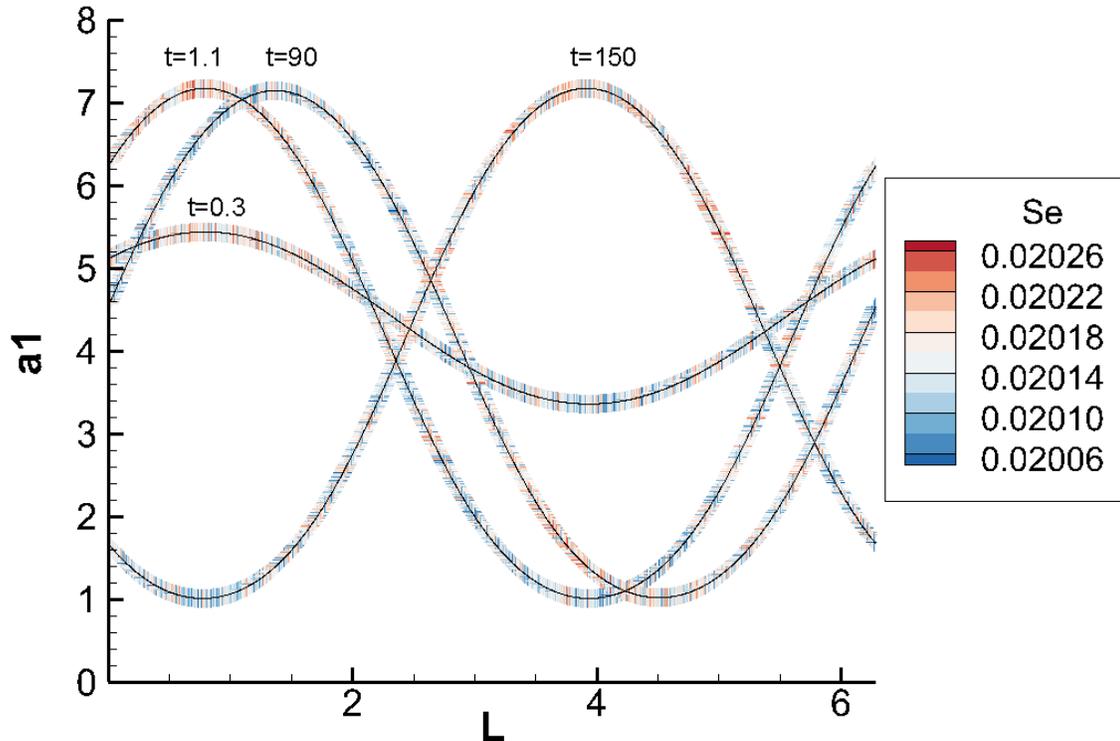
Figure 3.3: Response of the Meinhardt model on a stationary circle of radius 1 centred at $(0,0)$. The graph shows a_1 along the arc length at simulation times 0.3, 1.1, 90 and 150. The contour plot refers to s_e which started with a chemotactic signal at $(5,5)$ and changed to $(-5,-5)$ at time 15.

After that, at time 15 the signal was change to the opposite direction and the system needed about $t = 150$ to developed the new polarised state. The transition from $t = 1.1$ to $t = 150$ occurred as a travelling wave as indicated by the results at time 90.

3.5.2   Chemotactic cell migration

The simulation ran until $t = 158$ where although the cell did not reach the point $(0, 10)$ it showed a clear tendency. Therefore we can see the ability of the model to reproduce migration to specific locations and adaption to new signalling sources. Fig. 3.4 shows the changes in shape and position of the cell as well as the a_b field. In this case, the domain conserved a round-like shape throughout the complete simulation. Further, in Fig. 3.5 the trajectory of the centroid during the simulation is presented. Here, it can be notice that at the beginning the cell took some time to adapt to the initial signal but eventually it migrated with a clear direction, from around $(2.4, 1)$ to the signalling-source point $(5, 5)$. With respect to the response of the Meinhardt model with the signal an parameters used, we can see, by means of the a_b field, that it adapts to the signalling sources.

Finally, Fig. 3.6 shows the mesh quality and the behaviour of the mesh smoothing
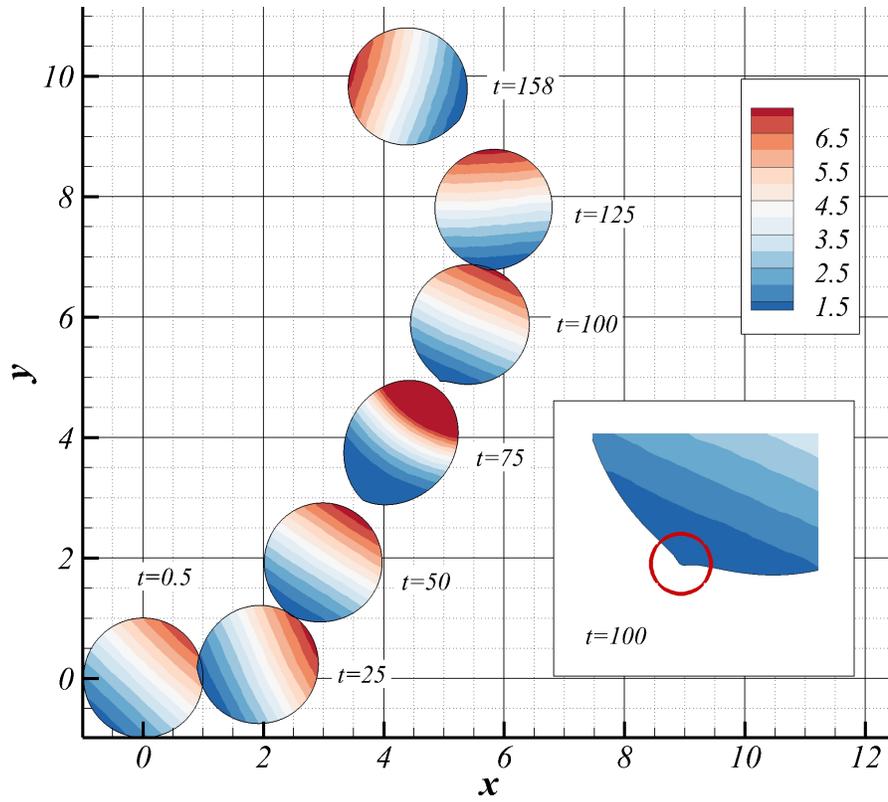
Figure 3.4: Results of chemotactic cell migration at $t = 0.5, 25, 50, 75, 100, 125, 158$. The colour map indicates the a_b field.
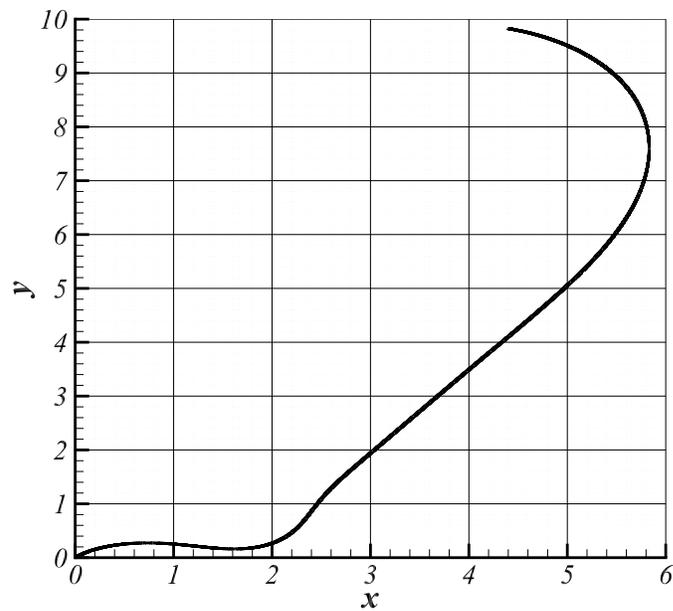

Figure 3.5: Tracking of the centroid of the cell in chemotactic migration.

and remeshing schemes. For the former, Fig. 3.6a shows from top to bottom the maximum, the average and the minimum qualities, respectively, throughout the simulation. The maximum was 1 at every step, which is in fact the maximum quality possible. The average remained around 0.96, this is a high quality value and indicates that the mesh throughout the simulation was good. In contrast, the minimum quality fluctuated significantly with a lowest value at about 0.58 and a highest at about 0.69. Regarding the activity of the smoothing and remeshing schemes, the former needed 4 or 5 iterations at almost every step and the latter was used 10 times. In this case, the smoothing scheme was efficient for around 15000 steps. Additionally, in the figure it is noticeable that the space between remeshing schemes was rather regular.

### 3.5.3   Spontaneous cell movement

Fig. 3.7 shows the trajectory of the cell centroid which indicates zigzag turning and some directional persistence. In Fig. 3.8 the shape and the a_b field are illustrated at $t = 0.5, 12.5, 25, 37.5, 50, 67.5$. Although the deformation of the domain is higher than in the previous case, it is noticeable how the round-like shape is still dominant. In addition, the commonly reported behaviour of the Meinhardt model can be seen, i.e., the appearance of two competing pseudopods (Campbell et al., 2017; Elliott et al., 2012; Meinhardt, 1999; Neilson et al., 2011).

Lastly, Fig. 3.9 describes the quality of the mesh throughout the simulation. Although the maximum quality was again 1, the average and the minimum qualities fluctuated more and reached lower values compared with the chemotactic case. Further, Fig. 3.9b shows two stages. At the beginning, until about $t = 20$, the smoothing scheme was sufficiently enough to deal with the mesh deformation. However, after $t = 20$ the it was not as efficient and in fact many more runs of the remeshing scheme were needed.

3.6   Discussion

In this section we shall discuss the results of the computational implementation. First, we saw that the Meinhardt model yielded a travelling wave, chemotactic case, and (ii) competing peaks, spontaneous case, along the membrane. Although the dynamics of the leading edge varies from cell to cell, most cells have travelling actin waves (Allard and Mogilner, 2013). These waves can appear locally or globally, depending on the cell and the migration environment. In chemotactically migrating cells the waves appear locally and help cells to avoid obstacles or reorient (Allard and Mogilner, 2013). Fig. 3.10 illustrates this phenomenon in human breast cancer (MDA-MB-231 line). By following the arrows, which indicate the position of the leading edge, we can appreciate the travelling wave from Fig. 3.10a to Fig. 3.10d. This phenomenon where the leading edge travels from one location to another is successfully mimicked in our chemotactic system, as shown in Fig. 3.4.

In contrast, when cells move unsteadily the actin dynamics can include global
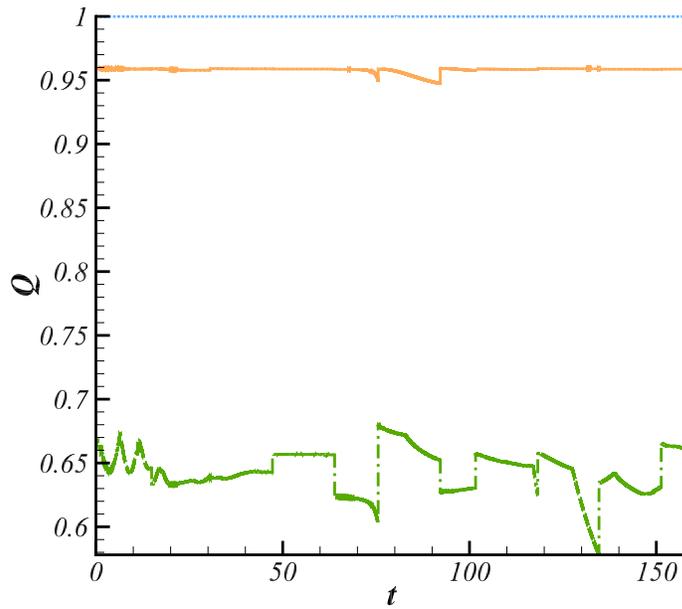
g

(a) Mesh quality statistics. From top to bottom the curves indicate respectively the maximum, the average and the minimum qualities.
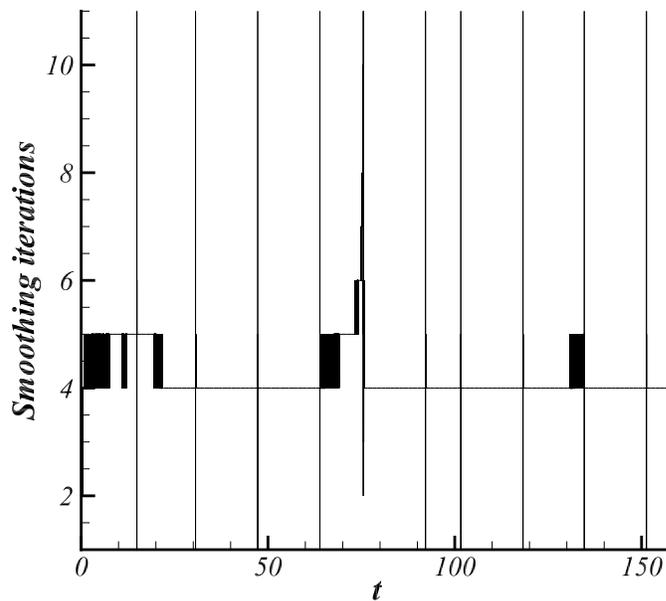
(b) Number of smoothing iterations. The vertical lines indicate a remeshing step.

Figure 3.6: Report of mesh statistics and smoothing iterations at each step in chemotactic migration.
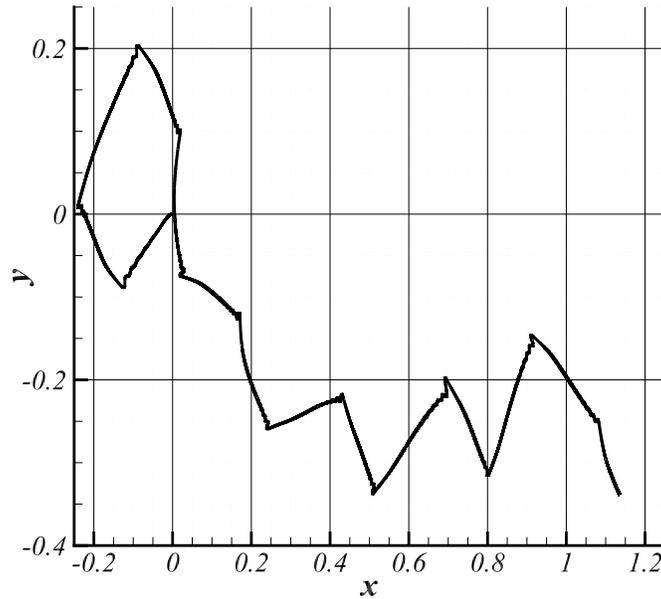
Figure 3.7: Tracking of the centroid of the cell in spontaneous migration.

travelling waves and the appearance of leading edges at different locations (Allard and Mogilner, 2013). In Fig. 3.8, the spontaneous-migration case reproduces this type of kinetic dynamics, as also reported in (Campbell et al., 2017; Elliott et al., 2012; Neilson et al., 2011). Nonetheless, in the case presented here, the parameters are all homogeneous and thus the kinetics is completely spontaneous. For instance, the models presented in (Elliott et al., 2012; Neilson et al., 2011) include a space-dependent chemotactic-signalling term and, even though the work in (Campbell et al., 2017) dealt with random migration, the authors also include a space-dependent random-signalling term. The dissimilarity in our chemotactic response therefore is due to the difference in parameters and the signalling term. Nonetheless, even though the model can reproduce chemotactic and spontaneous migration, it utilises different parameters in each scenario; thus, a further analysis of the model is required. It would be very interesting to find a set of parameters able to provide a local travelling wave in chemotactic migration as well as competing peaks in spontaneous migration.

In addition, our results show a marked round-like shape. This is common in amoeboid movement which characterises by small or highly homogeneously distributed adhesion points and strong actomyosin-mediated contractility (Friedl and Alexander, 2011). In the model, the adhesion points are represented by the right-hand-side term of Eq. (3.13) which is space-independent. The contraction, dominated by λ, is also homogeneous and therefore does not precisely model actomyosin-mediated contractility because λ is not polarised. Yet, it does contribute to maintain the round shape of the domain as does such mechanism. Additionally, at time
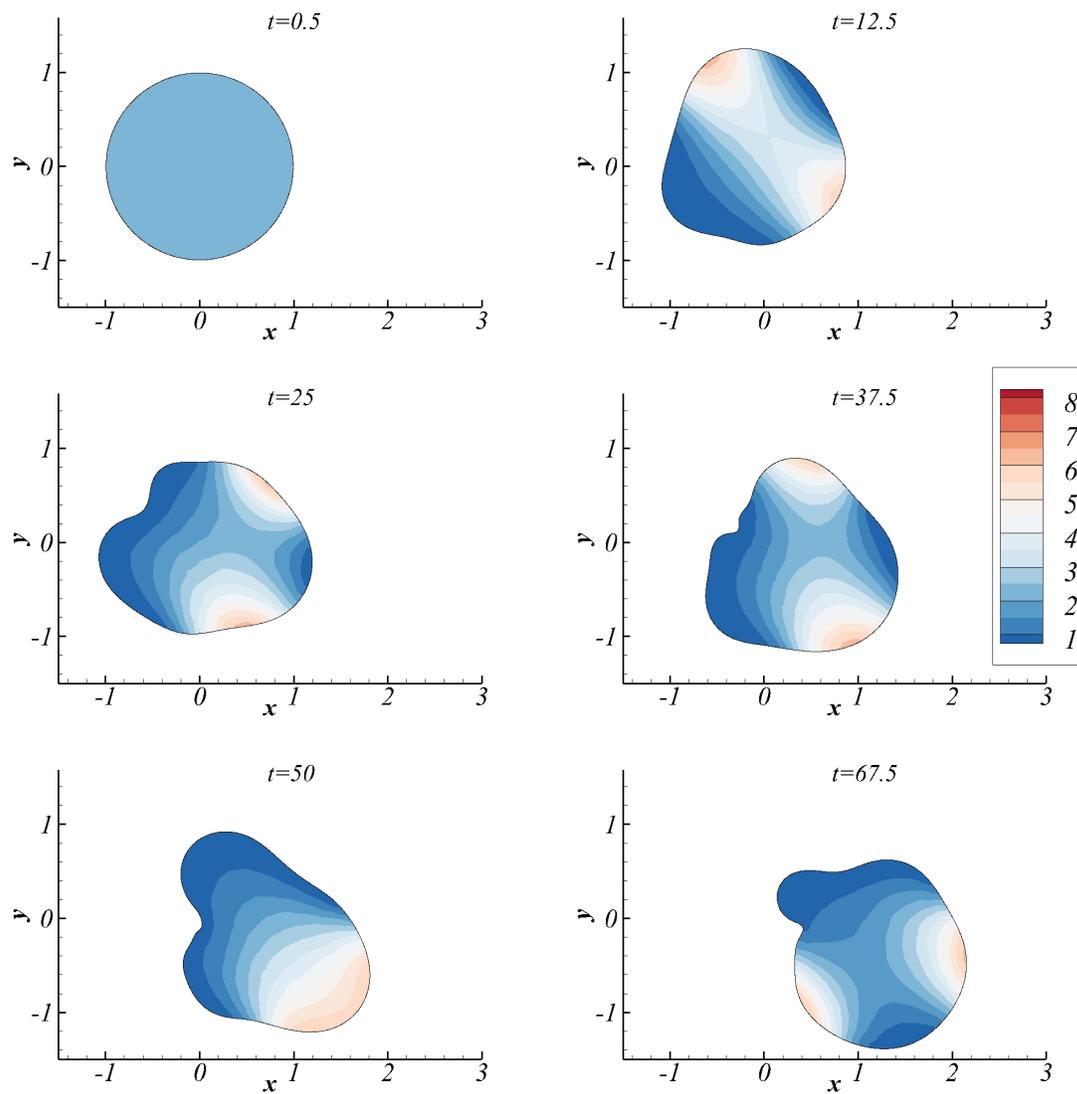
Figure 3.8: Results of spontaneous cell migration at $t = 0.5, 12.5, 25, 37.5, 50, 67.5$. The colour map indicates the a_b field.
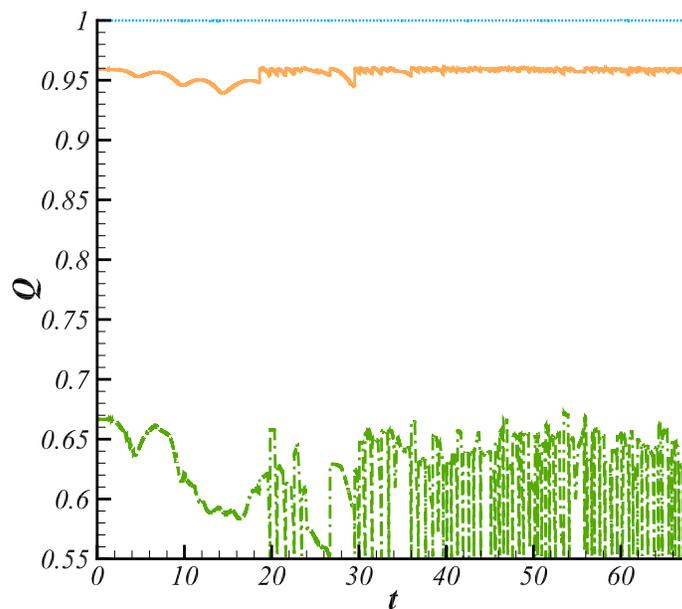
(a) Mesh quality statistics. From top to bottom the curves indicate respectively the maximum, the average and the minimum qualities.
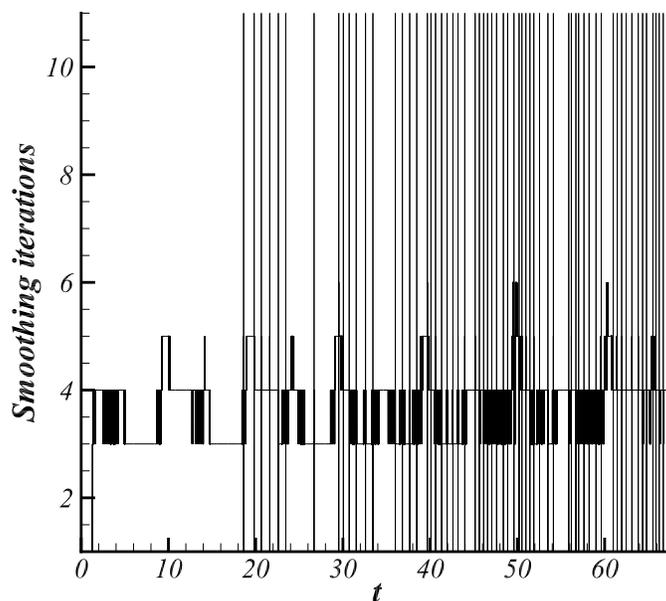
(b) Number of smoothing iterations. The vertical lines indicate a remeshing step.

Figure 3.9: Report of mesh statistics and smoothing iterations at each step in spontaneous migration.

(a)

(b)

(c)

(d)
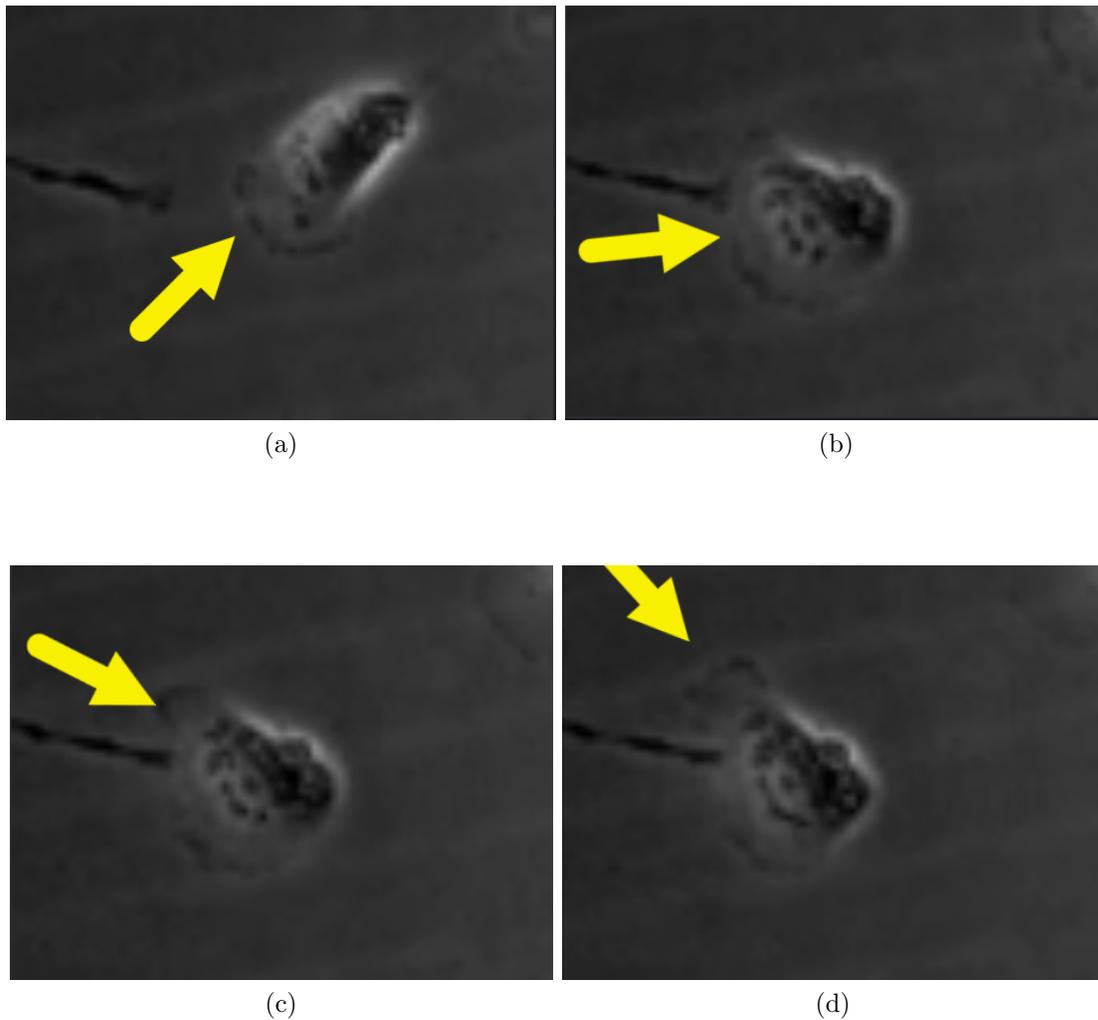
Figure 3.10: Picture shots from the cell migration assay using human breast cancer (MDA-MB-231 line) presented in (Gau and Roy, 2020) (permission given by Dr. Gau). The arrows point to the leading edge and show how it travels along the membrane.

$t = 100$ of the chemotactic case, we can see that the rear has a small protuberance which can be also appreciated in Fig. 3.10c. Although the protuberance in the simulation is not as large as that it the experiment, it indicates that the movements are similar.

In the case of spontaneous migration, the trajectory (Fig. 3.7) exhibits zigzag turning and some directional persistence. Da Yang et al. (2011) describes this phenomenon for microglia cells from rats (PMG) and mice (MG5). In their experiments, cells were able to move freely, without external guidance and at a very low density, and showed a tendency to advance in an almost linear straight direction followed by a sudden changed in direction. Further, they determined a statistically significant zigzag pattern. In short, they showed that it is more likely that a microglia cell will turn in the opposite direction of the previous turn than in the same direction. In other words, after turning with a positive angle it is more likely that the cell will turn with a negative angle and the other way around. In addition, they also reported a short-term directional persistence. This response of the Meinhardt model has been previously reported in (Elliott et al., 2012; Neilson et al., 2011).

Chapter 4

Conclusions and Future Work

In this work a computational tool for the simulation of cell migration was introduced. The implementation counts with the following key features: spontaneous and forced membrane polarisation, downstream polarisation within the cytoplasm, and mechanical responses due to the cytoskeleton dynamics. In particular, the Meinhardt's model for cell orientation was used to model the first feature, the second was model by means of a linear diffusion-depletion model, and the last was model by elastic deformation with no accumulation of elastic energy. Mathematically, the mechanical model can be regarded as a thermal expansion and contraction system with elastic supports all over the domain and curvature-dependent forces on the contour. Under the biological perspective, expansion and contraction occur as a consequence of the dynamics of the actin cytoskeleton and myosin proteins. In addition, elastic supports refer to focal adhesions and the curvature-dependent forces represent the membrane tension. In terms of the numerical implementation, the computational tool deals with highly deforming domains by means of three algorithms: the de Boor (1973)'s algorithm to equidistribute the boundary mesh, the Durand et al. (2019)'s algorithm to smooth the bulk mesh, and the Engwirda (2005, 2014)'s toolbox to remesh the domain when necessary. Further, the delivered computational tool is able to simulate bulk-surface phenomena in evolving two-dimensional domains yet it would require the modification of the model equations.

The novelty of the presented work lies in: the thermal expansion approach of the mechanical response and the implementation of the completely moving two-dimensional framework. Previous works utilised only forces on the boundary to drive movement while in this case, forces appear in the whole domain. We consider such forces assuming that the actin polymerisation generates forces along all the actin network. Further, although there are several models for cell migration, most of them do not include an evolving bulk-surface domain. In addition, we also improved the Durand et al. (2019)'s algorithm by combining it with the de Boor (1973)'s algorithm. Durand et al. (2019), in their paper, indicated that non-straight surface meshes, for example a circle, could not be smoothed with their algorithm; however, the de Boor (1973)'s algorithm presented here, easily deals with any sort of surface.

Nonetheless, this is more a first step towards cell migration simulation and prediction. The model has several limitations including:

- The mechanical behaviour is purely elastic.

- The dynamics of the different molecules interacting within the cell and the plasma membrane does not directly represent the species.

- The focal adhesions in a cell are located at different places but not everywhere as assumed here.

Thus, future work could be focused on:

- More complex mechanical models, for example, the implementation of visco-elasticity or hyper-elasticity theories.

- The development of biologically-inspired cytosolic and membrane kinetics and communication, for example, the formulation of bulk-surface PDE where the variables directly represent specific molecules.

- Different ways to model focal adhesions, for instance, since they do not appear everywhere and are constantly degraded, a stochastic equation could describe their location and a reaction equation their strength, Ψ.

- A more discrete modelling of the cytosolic and membrane kinetics, for example, active and inactive GPCR's could be regarded as discrete entities able to modify the actin cytoskeleton at specific locations.

- The inclusion of the bending forces on the membrane.

Appendix A

Numerical Model

A.1 The evolving surface finite element method (ESFEM)

Let us start by presenting the ESFEM following (Barreira et al., 2011; Frittelli et al., 2018). First, we shall write the weak form of Eq. (3.8). By multiplying it by a test function ϕ and integrating it over $\Gamma(t)$, that gives:

$$\int_{\Gamma(t)} \phi\partial^\bullet a_k + \int_{\Gamma(t)} \phi a_k \nabla_{\Gamma(t)} \cdot \mathbf{v} - d_k \int_{\Gamma(t)} \phi\Delta_{\Gamma(t)} a_k = \int_{\Gamma(t)} \phi f_k(\boldsymbol{a}). \tag{A.1}$$

Assuming either $\Gamma(t)$ is a closed surface, or zero flux boundary conditions, or $\phi(\partial\Gamma(t)) = 0$ and applying Green's theorem to the third term of the left-hand side of the equation leads to:

$$\int_{\Gamma(t)} \phi\partial^\bullet a_k + \int_{\Gamma(t)} \phi a_k \nabla_{\Gamma(t)} \cdot \mathbf{v} + d_k \int_{\Gamma(t)} \nabla_{\Gamma(t)}\phi \cdot \nabla_{\Gamma(t)} a_k = \int_{\Gamma(t)} \phi f_k(\boldsymbol{a}). \tag{A.2}$$

Replacing $\phi\partial^\bullet a_k = \partial^\bullet(\phi a_k) - a_k\partial^\bullet\phi$ yields to:

$$\int_{\Gamma(t)} (\partial^\bullet(\phi a_k) - a_k\partial^\bullet\phi) + \int_{\Gamma(t)} \phi a_k \nabla_{\Gamma(t)} \cdot \mathbf{v} + d_k \int_{\Gamma(t)} \nabla_{\Gamma(t)}\phi \cdot \nabla_{\Gamma(t)} a_k = \int_{\Gamma(t)} \phi f_k(\boldsymbol{a}). \tag{A.3}$$

Finally, following the transport formula Eq. (3.3) for ϕa_k, the weak form is given by: find $a_k(\boldsymbol{x}, t) \in H^1(\Gamma(t))$ such that

$$\frac{\mathrm{d}}{\mathrm{d}t}\int_{\Gamma(t)} \phi a_k - \int_{\Gamma(t)} a_k\partial^\bullet\phi + d_k \int_{\Gamma(t)} \nabla_{\Gamma(t)}\phi \cdot \nabla_{\Gamma(t)} a_k = \int_{\Gamma(t)} \phi f_k(\boldsymbol{a}), \ \forall\phi \in H^1(\Gamma(t)), \tag{A.4}$$

where $H^1(\Omega)$ is the Hilbert space defined at Ω.

Before deriving the ESFEM, let us take into account the following considerations:

- The surface $\Gamma(t)$ will be approximated by a piecewise linear surface $\Gamma^h(t) \ni \mathbf{r}(t)$. This discrete surface is composed by a set of N^s nodes $\mathbf{x}_m(t)$, $m =$

$1, ..., N^s$, and E^s elements (subdomains) $\Gamma_e^h(t)$, $e = 1, ..., E^s$, such that:

$$\Gamma^h(t) = \bigcup_{e=1}^{E_s} \Gamma_e^h(t)$$

and the intersection between two different elements is either a node or null.

- Since the following holds:

$$\frac{\mathrm{d}}{\mathrm{d}t}\int_{\Gamma^h(t)}(\cdot) = \frac{\mathrm{d}}{\mathrm{d}t}\left(\sum_{e=1}^{E^s}\int_{\Gamma_e^h(t)}(\cdot)\right) = \sum_{e=1}^{E^s}\left(\frac{\mathrm{d}}{\mathrm{d}t}\int_{\Gamma_e^h(t)}(\cdot)\right) \qquad \text{(A.5)}$$

  we might jump from a global formulation to a local formulation. This will be useful at formulating the Newton-Raphson scheme to be implemented in ABAQUS.

- The linear finite element space $V^h(\Gamma^h(t))$ will be the span of the N^s basis functions $\chi_j(\mathbf{r}(t), t)$. χ_j are piecewise linear functions such that $\chi_j(\mathbf{r}(t) = \mathbf{x}_i(t), t) = \delta_{ij}$.

- $a_k(\cdot, t)$ will be approximated by a piecewise linear function ${}^k\mathcal{A}(\mathbf{r}(t), t)$:

$$^k\mathcal{A}(\mathbf{r}(t), t) = \sum_{j=1}^{N^s} \chi_j(\mathbf{r}(t), t){}^k A_j(t) \qquad \text{(A.6)}$$

  where ${}^k A_j(t)$ are the approximated nodal values of $a_k(\cdot, t)$ on $\Gamma^h(t)$.

- The discrete test function ϕ^h is said to have the form of ${}^k\mathcal{A}$.

- In (Dziuk and Elliott, 2007) it was shown that:

$$\partial^\bullet \chi_i(\mathbf{r}(t), t) = 0. \qquad \text{(A.7)}$$

- The scheme for time discretisation will be the fully implicit Backward Euler method.

With the above considerations, the finite element problem is: find ${}^k\mathcal{A} \in V^h(\Gamma^h(t)$ such that:

$$\frac{\mathrm{d}}{\mathrm{d}t}\int_{\Gamma^h(t)} \phi^{h\,k}\mathcal{A} - \int_{\Gamma^h(t)} {}^k\mathcal{A}\partial^\bullet\phi^h + d_k \int_{\Gamma^h(t)} \nabla_{\Gamma^h(t)}\phi^h \cdot \nabla_{\Gamma^h(t)}{}^k\mathcal{A}$$

$$= \int_{\Gamma^h(t)} \phi^h f_k({}^1\mathcal{A}, ..., {}^w\mathcal{A}), \ \forall \phi^h \in V^h(\Gamma^h(t)). \qquad \text{(A.8)}$$

Applying Eq. (A.6) and since ϕ^h has the same form as $^k\mathcal{A}$ we get the following problem: find $^k\boldsymbol{A}(t) \in \mathbb{R}^{N^s}$ such that:

$$\frac{\mathrm{d}}{\mathrm{d}t} \int_{\Gamma^h(t)} \sum_{i,j=1}^{N^s} \chi_i \chi_j\,^k A_j(t) - \sum_{i,j=1}^{N^s} \int_{\Gamma^h(t)} \chi_j\,^k A_j(t) \partial^\bullet(\chi_i)$$
$$+d_k \int_{\Gamma^h(t)} \sum_{i,j=1}^{N^s} \nabla_{\Gamma^h(t)} \chi_i \cdot \nabla_{\Gamma^h(t)} \chi_j\,^k A_j(t) = \int_{\Gamma^h(t)} \sum_i^{N^s} \chi_i f_k(^1\boldsymbol{A}, ..., ^w\boldsymbol{A}). \tag{A.9}$$

Recalling Eq. (A.7) yields to:

$$\frac{\mathrm{d}}{\mathrm{d}t} \int_{\Gamma^h(t)} \sum_{i,j=1}^{N^s} \chi_i \chi_j\,^k A_j(t) + d_k \int_{\Gamma^h(t)} \sum_{i,j=1}^{N^s} \nabla_{\Gamma^h(t)} \chi_i \cdot \nabla_{\Gamma^h(t)} \chi_j\,^k A_j(t)$$
$$= \int_{\Gamma^h(t)} \sum_{i=1}^{N^s} \chi_i f_k(^1\boldsymbol{A}, ..., ^w\boldsymbol{A}). \tag{A.10}$$

Finally, defining the mass matrix as:

$$\mathcal{M}_{ij}(t) = \int_{\Gamma^h(t)} \chi_i\big(\mathbf{r}(t)\big) \chi_j\big(\mathbf{r}(t)\big),$$

the stiffness matrix as:

$$\mathcal{S}_{ij}(t) = \int_{\Gamma^h(t)} \nabla_{\Gamma^h(t)} \chi_i\big(\mathbf{r}(t)\big) \cdot \nabla_{\Gamma^h(t)} \chi_j\big(\mathbf{r}(t)\big),$$

and the reaction vector as:

$$^k\mathcal{F}_i(t) = \int_{\Gamma^h(t)} \chi_i\big(\mathbf{r}(t)\big) f_k\big(\boldsymbol{A}\big),$$

the ESFEM for the kth species is given by:

$$\frac{\mathrm{d}}{\mathrm{d}t} \big(\mathcal{M}_{ij}(t)^k A_j(t)\big) + d_k \mathcal{S}_{ij}(t)^k A_j(t) = {}^k\mathcal{F}_i(t). \tag{A.11}$$

We now can derive the fully-implicit system. Applying the Backward-Euler scheme for time integration Eq. (A.11) becomes:

$$\frac{1}{\tau} \left(\mathcal{M}_{ij}{}^{n+1k} A_j{}^{n+1} - \mathcal{M}_{ij}{}^{nk} A_j{}^n\right) + d_k \mathcal{S}_{ij}{}^{n+1k} A_j{}^{n+1} = {}^k\mathcal{F}_i{}^{n+1}, \tag{A.12}$$

where τ is the discrete time step, the superscripts $(\cdot)^{n+1}$ and $(\cdot)^n$ refer to the solution at time $(n+1)\tau$ and the solution at time $n\tau$, respectively.

The right-hand-side of Eq. (A.12) is in general nonlinear, as in the Meinhardt model for cell polarisation. Hence, the Newton-Raphson method might be necessary.

Since we will implement it in ABAQUS it is convenient to jump to a local formulation by Eq. (A.5). Then, let us rewrite the system as:

$$\sum_{e=1}^{E^s} \left(\frac{1}{\tau} \left({}_e\mathcal{M}_{ij}^{n+1} {}_e^k A_j^{n+1} - {}_e\mathcal{M}_{ij}^n {}_e^k A_j^n \right) + d_k {}_e\mathcal{S}_{ij}^{n+1} {}_e^k A_j^{n+1} - {}_e^k\mathcal{F}_i^{n+1} \right) = \sum_{e=1}^{E^s} \left({}_e^k R_i \right),$$

(A.13)

where the superscripts ^{e} indicate local versions of the arrays and ${}_e^k R_i$ are local residuals. For this system the tangent stiffness matrix is given by:

$$\sum_{e=1}^{E^s} \left(\frac{\partial {}_e^k R_i}{\partial {}_e^k A_l^{n+1}} \right) = \sum_{e=1}^{E^s} \begin{cases} \frac{1}{\tau}\mathcal{M}_{ij}^{e\,n+1} + d_k {}_e\mathcal{S}_{ij}^{n+1} - \dfrac{\partial {}_e^k\mathcal{F}_i^{n+1}}{\partial {}_e^k A_l^{n+1}} & \text{for } k = l, \text{ and} \\[2ex] -\dfrac{\partial {}_e^k\mathcal{F}_i^{n+1}}{\partial {}_e^k A_l^{n+1}} & \text{for } k \neq l, \end{cases}$$

(A.14)

where

$$\frac{\partial {}_e^k\mathcal{F}_i^{n+1}}{\partial {}_e^k A_l^{n+1}} = \int_{\Gamma_h^e(t)} \chi_i^{n+1}\chi_j^{n+1}\frac{\partial f_k}{\partial A_l^{n+1}}$$

(A.15)

Matrices ${}_e\mathcal{M}_{ij}(t)$ and ${}_e\mathcal{S}_{ij}(t)$ are analytically integrated, and the reactive matrices and vectors are numerically integrated by Gaussian quadrature.

A.2   Finite element method in the bulk

Let us now write the variational problem of Eq. (3.26): find $a_b \in H^1(\Omega)$ such that:

$$0 = \int_\Omega \left(\varphi \left(d_b\Delta a_b - C_b a_b \right) \right) \ \forall\varphi \in H^1(\Omega),$$

(A.16)

with φ a test function. Applying Green's theorem, the weak problem reads: find $a_b \in H^1(\Omega)$ such that:

$$0 = \int_\Gamma \varphi\nabla a_b - d_b \int_\Omega \nabla\varphi\nabla a_b - \int_\Omega \varphi C_b a_b \ \forall\varphi \in H^1(\Omega).$$

(A.17)

We now need an appropriate finite element space. First, we can discretise Ω by a triangulation $\mathscr{T}^h$ composed of N^b nodes $\mathbf{x}_i$ and E^b triangles T_e. Then the finite element space $V^h(\Omega^h) := \text{span}\{\zeta_j\}_{j=1}^{N^b}$ where $\zeta_j(\mathbf{x}_i) = \delta_{ij}$ and $\zeta_j|_{T_e}$ is affine. The finite element problem then reads: find ${}^b\mathcal{A} \in V^h(\Omega^h)$ such that:

$$0 = \int_{\Gamma^h} \varphi^h\nabla\,{}^b\mathcal{A} - d_b \int_{\Omega^h} \nabla\varphi^h\nabla\,{}^b\mathcal{A} - \int_{\Omega^h} \varphi^h C_b\,{}^b\mathcal{A} \qquad \forall\varphi^h \in V^h.$$

(A.18)

where a_b is the piecewise linear approximation of a_b and φ^h is a discrete test function.

Since φ^h and ${}^b\mathcal{A}$ are linear combinations of $\{\zeta_j\}_{j=1}^{N^b}$, we can rewrite Eq. (A.18) as

the algebraic problem: find $^b\mathbf{A} \in \mathbb{R}^{N^b}$ such that:

$$0 = \int_{\Gamma^h} \sum_{i,j=1}^{N^b} \left(\zeta_j \nabla \zeta_i \, ^b A_i\right) - d_b \int_{\Omega^h} \sum_{i,j=1}^{N^b} \left(\nabla \zeta_j \nabla \zeta_i \, ^b A_i\right) - \int_{\Omega^h} \sum_{i,j=1}^{N^b} \left(\zeta_j C_b \, ^b A_i\right), \quad \text{(A.19)}$$

where $^b A_i$ are the components of $^b\mathbf{A}$. We know $^b\mathcal{A}$ on the surface from Eq. (3.26), then the first term of the right-hand-side is known.

Finally, to compute the integrals let us define a reference element and its linear basis functions. Consider a reference element described by the vertices: $(0,0)$, $(1,0)$ and $(0,1)$. If this element lives in a Cartesian space ξ, η then the basis functions within a triangle are given by:

$$_e\zeta_1 = 1 - \xi - \eta, \tag{A.20}$$
$$_e\zeta_2 = \xi, \tag{A.21}$$
$$_e\zeta_3 = \eta. \tag{A.22}$$

We can then have a transformation from any element, with vertices $_e\mathbf{x}_i = (x_i^e, y_i^e)$, $i = 1, 2, 3$, to the reference element by the transformation with Jacobian:

$$J_b = (_ex_2 - {_ex_1})(_ey_3 - {_ey_1}) - (_ex_3 - {_ex_1})(_ey_2 - {_ey_1}), \tag{A.23}$$

which is twice the area.

A.3 Finite element approximation of the mean curvature vector

Let us define $\boldsymbol{H}^1(\Gamma) := H^1(\Gamma) \times H^1(\Gamma)$. Then, the variational formulation of Eq. (3.15) reads: find $\boldsymbol{\kappa} \in \boldsymbol{H}^1(\Gamma)$ such that:

$$\int_\Gamma \boldsymbol{\vartheta} \cdot \boldsymbol{\kappa} = -\int_\Gamma \boldsymbol{\vartheta} \cdot \Delta_\Gamma \boldsymbol{x} \qquad \forall \boldsymbol{\vartheta} \in \boldsymbol{H}^1(\Gamma). \tag{A.24}$$

For closed curves and applying Green's theorem, the weak problem reads: find $\boldsymbol{\kappa} \in \boldsymbol{H}^1(\Gamma)$ such that:

$$\int_\Gamma \boldsymbol{\vartheta} \cdot \boldsymbol{\kappa} = \int_\Gamma \nabla_\Gamma \boldsymbol{\vartheta} \cdot \nabla_\Gamma \boldsymbol{x} \qquad \forall \boldsymbol{\vartheta} \in \boldsymbol{H}^1(\Gamma). \tag{A.25}$$

From (Heine, 2004), the finite element approximation of the curvature mean vector problem is not convergent when using linear elements, however, it is first-order convergent when using quadratic elements, second-order convergent when using cubic elements and so on. Therefore, we shall construct at least a quadratic finite element space. Let us then set a triangulation $\mathcal{Q}^h$ for Γ composed of N^s nodes $\mathbf{x}_m$ and E^q segments L_e^q, which composes the piecewise-quadratic surface Γ^q. The finite element space is $Q^h := \text{span}\{\theta_j\}_{j=1}^{N^s}$ where $\theta_j(\mathbf{x}_i) = \delta_{ij}$ and $\theta_j|_{L_e^q}$ is either zero or

quadratic. If we define $\boldsymbol{Q}^h := Q^h \times Q^h$ the finite element problem then reads: find $\boldsymbol{\kappa}^h \in \boldsymbol{Q}^h$ such that:

$$\int_{\Gamma^q} \boldsymbol{\vartheta}^h \cdot \boldsymbol{\kappa}^h = \int_{\Gamma^q} \nabla_{\Gamma^q} \boldsymbol{\vartheta}^h \cdot \nabla_{\Gamma^q} \boldsymbol{x}^h \qquad\qquad \forall \boldsymbol{\vartheta}^h \in \boldsymbol{Q}^h. \qquad (A.26)$$

Notice that $\boldsymbol{x}^h$ in Eq. (A.26) indicates an isoparameterisation of the surface. From the definition of $\mathscr{Q}^h$ we can write $\boldsymbol{\kappa}^h$ and $\boldsymbol{x}^h$ as:

$$\boldsymbol{\kappa}^h = \sum_{j=1}^{N^s} \theta_j \mathbf{K}_j, \qquad (A.27)$$

$$\boldsymbol{x}^h = \sum_{i=1}^{N^s} \theta_i \mathbf{x}_i, \qquad (A.28)$$

where $\mathbf{K}$ is the nodal mean curvature vector. Replacing Eqs. (A.27) and (A.28) into Eq. (A.26) yields the following algebraic problem: find $\mathbf{K} \in \mathbb{R}^{2N^s}$ such that:

$$\int_{\Gamma^q} \sum_{k,j=1}^{N^s} \theta_k \theta_j \mathbf{K}_j = \int_{\Gamma^q} \sum_{k,i=1}^{N^s} \nabla_{\Gamma^q} \theta_k \nabla_{\Gamma^q} \theta_i \mathbf{x}_i. \qquad (A.29)$$

Lastly, since we need Q^h be a space of piecewise functions of at least quadratic order, let us define the quadratic set of basis functions. We can use a one-dimensional reference element from -1 to 1 with a middle node at 0. If we associate ξ as the coordinate of this reference element, the basis functions within a three-node element are:

$$_e\theta_1 = 0.5\xi(\xi - 1), \qquad (A.30)$$

$$_e\theta_2 = 0.5\xi(\xi + 1), \qquad (A.31)$$

$$_e\theta_3 = 1 - \xi^2. \qquad (A.32)$$

We can then define a transformation from any element, with nodes $(_ex_1, {}_ey_1)$, $(_ex_2, {}_ey_2)$ and $(_ex_3, {}_ey_3)$ (the middle node) to the reference element by the transformation with Jacobian:

$$J_q = \sqrt{\left(\sum_{i=1}^{3} \frac{d\,_e\phi_i}{d\xi}\,_ex_i\right)^2 + \left(\sum_{i=1}^{3} \frac{d\,_e\phi_i}{d\xi}\,_ey_i\right)^2}. \qquad (A.33)$$

A.4   Finite element approximation of the mechanical model

Let us write the variational problem for Eq. (3.13): find $\boldsymbol{u} \in \boldsymbol{H}^1(\Omega)$ such that:

$$\int_{\Omega} \boldsymbol{\varphi} \cdot (\nabla \cdot (\boldsymbol{\sigma} - \boldsymbol{\sigma_p} + \boldsymbol{\sigma_c})) = \int_{\Omega} \boldsymbol{\varphi} \cdot \Psi \boldsymbol{u} \qquad \forall \boldsymbol{\varphi} \in \boldsymbol{H}^1(\Omega). \qquad (A.34)$$

Applying Green's theorem to the left-hand-side of the equation the weak form reads: find $\boldsymbol{u} \in \boldsymbol{H}^1(\Omega)$ such that:

$$\int_\Gamma \boldsymbol{\varphi} \cdot (\boldsymbol{\sigma} - \boldsymbol{\sigma_p} + \boldsymbol{\sigma_c}) \cdot \boldsymbol{n} - \int_\Omega \nabla\boldsymbol{\varphi} \cdot (\boldsymbol{\sigma} - \boldsymbol{\sigma_p} + \boldsymbol{\sigma_c}) = \int_\Omega \boldsymbol{\varphi} \cdot \Psi\boldsymbol{u} \quad \forall\boldsymbol{\varphi} \in \boldsymbol{H}^1(\Omega).$$

$$(A.35)$$

Replacing Eq. (3.14) and Eq. (3.21) into Eq. (A.35), we can rewrite the problem as: find $\boldsymbol{u} \in \boldsymbol{H}^1(\Omega)$ such that:

$$\int_\Gamma \boldsymbol{\varphi} \cdot \delta\lambda\boldsymbol{\kappa} - \int_\Omega \nabla\boldsymbol{\varphi} \cdot (\boldsymbol{\sigma} - \boldsymbol{\sigma_p} + \boldsymbol{\sigma_c}) = \int_\Omega \boldsymbol{\varphi} \cdot \Psi\boldsymbol{u} \qquad \forall\boldsymbol{\varphi} \in \boldsymbol{H}^1(\Omega), \qquad (A.36)$$

which from Eq. (3.16) becomes: find $\boldsymbol{u} \in \boldsymbol{H}^1(\Omega)$ such that:

$$\int_\Gamma \boldsymbol{\varphi} \cdot \delta\lambda\boldsymbol{\kappa} - \int_\Omega \nabla\boldsymbol{\varphi} \cdot (\mathcal{D}\boldsymbol{\varepsilon} - \boldsymbol{\sigma_p} + \boldsymbol{\sigma_c}) = \int_\Omega \boldsymbol{\varphi} \cdot \Psi\boldsymbol{u} \qquad \forall\boldsymbol{\varphi} \in \boldsymbol{H}^1(\Omega). \qquad (A.37)$$

From this weak problem we can now build the finite element problem. First, let us recall the triangulation $\mathcal{T}^h$ and the finite element space V^h from Appendix A.2. We can then define $\boldsymbol{V}^h := V^h \times V^h$. Thus, the finite element problem reads: find $\boldsymbol{u}^h \in \boldsymbol{V}^h(\Omega^h)$ such that:

$$\int_{\Gamma^h} \boldsymbol{\varphi}^h \cdot \delta\lambda\boldsymbol{\kappa}^h - \int_{\Omega^h} \nabla\boldsymbol{\varphi}^h \cdot \left(\mathcal{D}\boldsymbol{\varepsilon}^h - \boldsymbol{\sigma_p} + \boldsymbol{\sigma_c}\right) = \int_{\Omega^h} \boldsymbol{\varphi}^h \cdot \Psi\boldsymbol{u}^h \quad \forall\boldsymbol{\varphi}^h \in \boldsymbol{V}^h(\Omega^h).$$

$$(A.38)$$

Finally, let us introduce the matrices $\boldsymbol{\zeta}$ and $\mathbf{B}$ as:

$$\boldsymbol{\zeta} = \begin{bmatrix} \zeta_1 & 0 & \zeta_2 & 0 & \dots & \zeta_{N^b} & 0 \\ 0 & \zeta_1 & 0 & \zeta_2 & \dots & 0 & \zeta_{N^b} \end{bmatrix}, \qquad (A.39)$$

$$\mathbf{B} = \begin{bmatrix} \dfrac{\partial\zeta_1}{\partial y_1} & 0 & \dfrac{\partial\zeta_2}{\partial y_1} & 0 & \dots & \dfrac{\partial\zeta_{N^b}}{\partial y_1} & 0 \\ 0 & \dfrac{\partial\zeta_1}{\partial y_2} & 0 & \dfrac{\partial\zeta_2}{\partial y_2} & \dots & 0 & \dfrac{\partial\zeta_{N^b}}{\partial y_2} \\ \dfrac{\partial\zeta_1}{\partial y_2} & \dfrac{\partial\zeta_1}{\partial y_1} & \dfrac{\partial\zeta_2}{\partial y_2} & \dfrac{\partial\zeta_2}{\partial y_1} & \dots & \dfrac{\partial\zeta_{N^b}}{\partial y_2} & \dfrac{\partial\zeta_{N^b}}{\partial y_1} \end{bmatrix}, \qquad (A.40)$$

then, we can transform the finite element problem into the algebraic problem: find $\mathbf{U} \in \mathbb{R}^{2N^b}$ such that

$$\int_\Gamma \boldsymbol{\zeta}^\top \lambda\mathbf{K} - \int_\Omega \mathbf{B}^\top \mathcal{D}\mathbf{B}\mathbf{U} - \int_\Omega (\boldsymbol{F_p} - \boldsymbol{F_c}) - \int_\Omega \boldsymbol{\zeta}^\top \Psi\mathbf{U} = 0, \qquad (A.41)$$

where:

$$\boldsymbol{F_p} = \mathbf{B}^\top a_b \mathcal{D} \begin{bmatrix} 1 \\ 1 \\ 0 \end{bmatrix}, \qquad (A.42)$$

$$\boldsymbol{F_c} = \mathbf{B}^\top \lambda\mathcal{D} \begin{bmatrix} 1 \\ 1 \\ 0 \end{bmatrix}, \qquad (A.43)$$

$$(A.44)$$

A.5   Mesh Smoothing Algorithms

Two mesh smoothing algorithms are used to improve the quality of the elements throughout the simulation. First a surface mesh equidistribution scheme is implemented by means of the De Boor's algorithm (de Boor, 1973) and the parametric quadratic mesh. Second, the Durand et al. (2019)'s algorithm is implemented to smooth the bulk mesh. Additionally, a remeshing scheme is also utilised in case this algorithm does not improve the mesh quality above a specific threshold. This scheme is based on the Mesh2D toolbox (Engwirda, 2005, 2014).

Since we defined a quadratic finite element mesh for the surface in Appendix A.3, we can use the quadratic parameterisation to equidistribute the mesh. To do this, we need to define a transformation from a reference element from -1 to 1 to each element of the piecewise quadratic curve Γ^q and to compute the arc length of each element. Then we can use the De Boor's algorithm to reorganise the nodes such that the distance between each pair of adjacent nodes is equal. After that, we can use the inverse transformation to reconstruct the curve. We might use several iterations to improve the equidistribution.

Let us start by defining the transformation and the element arc length. Let $_e\boldsymbol{x}_1$, $_e\boldsymbol{x}_2$ and $_e\boldsymbol{x}_3$ be respectively the start-, the end- and the middle-nodes of an element $(\Gamma^q)^e$. The transformation then is:

$$_e\boldsymbol{x}(\xi) = {_e\theta_1}(\xi)\,{_e\boldsymbol{x}_1} + {_e\theta_2}(\xi)\,{_e\boldsymbol{x}_2} + {_e\theta_3}(\xi)\,{_e\boldsymbol{x}_3}, \tag{A.45}$$

where $_e\theta_i$ are defined in Eqs. (A.30) to (A.32). The arc length of each element $_e\mathfrak{A}_l$ equals the integral of the Jacobian given in Eq. (A.33), that is:

$$_e\mathfrak{A}_l = \int_{-1}^{1} \sqrt{\left(\sum_{i=1}^{3} \frac{d\,_e\theta_i}{d\xi}\,_ex_i\right)^2 + \left(\sum_{i=1}^{3} \frac{d\,_e\theta_i}{d\xi}\,_ey_i\right)^2}\, d\xi, \tag{A.46}$$

which can be approximated by Gaussian quadrature as:

$$_e\mathfrak{A}_l \approx \sum_{p=1}^{N_{GP}} \left(\sqrt{\left(\sum_{i=1}^{3} \frac{d\,_e\theta_i}{d\xi}(\xi_p)x_i\right)^2 + \left(\sum_{i=1}^{3} \frac{d\,_e\theta_i}{d\xi}(\xi_p)y_i\right)^2}\, w_p\right), \tag{A.47}$$

where N_{GP} are the number of Gaussian points and ξ_p are those Gaussian points.

Let us now compute the total arc length:

$$\mathfrak{A}_l = \sum_{e=1}^{E^q} {_e\mathfrak{A}_l}. \tag{A.48}$$

Since we want an equidistant surface mesh each element must have $\mathfrak{A}_l/E^q$ arc length. Therefore, by the De Boor's algorithm we can find the node locations that equidistribute the mesh.

Let $\mathfrak{A}_l^{ze}$ be the arc length from the first node until the end of element e, e.g. if $e = 3$, $\mathfrak{A}_l^{z3} = \mathfrak{A}_l^1 + \mathfrak{A}_l^2 + \mathfrak{A}_l^3$. Since each element must have arc length $\mathfrak{A}_l/E^q$ we need to

find a new ${}_e\boldsymbol{x}_2$, say ${}_e\hat{\boldsymbol{x}}_2$, such that the new arc length is $\hat{\mathfrak{A}}_L^{z_e} = e\mathfrak{A}_l/E^q$. Thus, by De Boor's algorithm we need to find and element r such that: $\mathfrak{A}_l^{z_{r-1}} \leq (e\mathfrak{A}_l/E^q) \leq \mathfrak{A}_l^{z_r}$. This means that ${}_e\hat{\boldsymbol{x}}_2$ belongs to element r. Then we find: ${}_e\hat{\boldsymbol{x}}_2$ such that:

$$e\mathfrak{A}_l/E^q - \mathfrak{A}_l^{z_{r-1}} = \int_{-1}^{\xi({}_e\hat{\boldsymbol{x}}_2)} \sqrt{\left(\sum_{i=1}^{3} \frac{d\,_r\phi_i}{d\xi}\,_rx_i\right)^2 + \left(\sum_{i=1}^{3} \frac{d\,_r\phi_i}{d\xi}\,_ry_i\right)^2}\, d\xi. \qquad (A.49)$$

Again we can use Gaussian quadrature to approximate $\xi({}_e\hat{\boldsymbol{x}}_2)$, although we need to iterate several times. Once we have $\xi({}_e\hat{\boldsymbol{x}}_2)$ we can use Eq. (A.45) on element r to find ${}_e\hat{\boldsymbol{x}}_2$.

For the bulk mesh smoothing we can use the method introduced in (Durand et al., 2019). The smoothing is performed by solving a linear elasticity deformation where every element whose shape is not regular is considered to be strained. Therefore, the loads are proportional to that strain. For general geometries the boundary is fixed. Then the mathematical formulation is:

$$\nabla \cdot (\boldsymbol{\sigma} - \boldsymbol{\sigma_s}) = \mathbf{0}, \qquad (A.50)$$

$$\boldsymbol{u}(\boldsymbol{x}) = \mathbf{0}, \qquad (A.51)$$

where $\boldsymbol{\sigma_s}$ is the stress induced by the irregularity of the elements. Following the procedure of Appendix A.4 the algebraic problem is given by: find $\boldsymbol{U} \in \mathbb{R}^{2N_b}$ such that:

$$\int_{\Omega^h} \mathbf{B}^\top \mathcal{I}\mathbf{B}\mathbf{U} = \int_{\Omega^h} \boldsymbol{F_s}, \qquad (A.52)$$

where $\mathcal{I}$ is the three-dimensional identity matrix and $\boldsymbol{F_s}$ is the force induced by the strain given by:

$$\boldsymbol{F_s} = \mathbf{B}^\top \mathcal{I}\mathbf{B}\boldsymbol{U}^\star, \qquad (A.53)$$

and $\boldsymbol{U}^\star$ are the nodal displacements from the irregular triangles to reference regular triangles, see Fig. A.1. In addition, in Fig. A.1 is the best fitting regular reference element whose vertices can be found by a least-square method.

As can be seen, the displacements in Fig. A.1 are local. To build $\boldsymbol{U}^\star$ we only need to sum all the local displacements of a node.

Furthermore, the method can be modified to improve the minimum quality $\mathscr{Q}_{\min}$ in expense of the average quality. Let us start by defining the metric. For a triangle it is given by (Durand et al., 2019):

$$\mathscr{Q}_T = \left(\frac{6\sqrt{\dfrac{\mathfrak{a}_T}{\sqrt{3}}}}{\mathfrak{p}_T}\right)^2, \qquad (A.54)$$

where $\mathfrak{a}_T$ and $\mathfrak{p}_T$ are respectively the area and perimeter of the triangle. The numerator equals the perimeter of a regular triangle with area $\mathfrak{a}$. To improve the
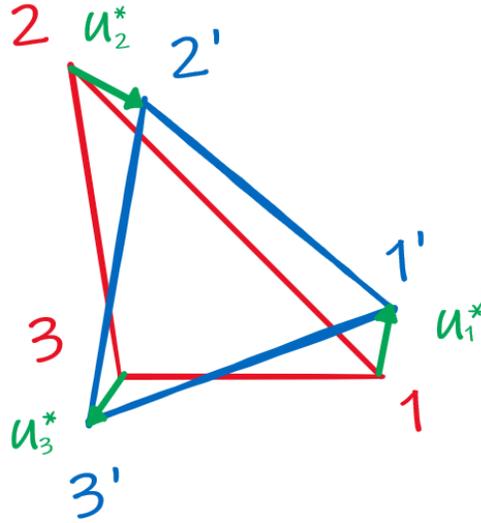
Figure A.1: Displacements (green arrows) from an irregular triangle (red triangle) to a regular triangle (blue triangle).

minimum quality, we can multiply the local displacements by:

$$\frac{1 - \mathcal{Q}}{1 - \mathcal{Q}_{\mathrm{min}}}.$$

Therefore, elements with less quality are prioritised.

Finally, if this method fails in improving $\mathcal{Q}_{\mathrm{min}}$ above some threshold, say $\mathcal{Q}^{\star}_{\mathrm{min}}$, we can use the Mesh2D toolbox (Engwirda, 2005, 2014) to remesh the domain. Since the bulk variables are not solve in a time dependent fashion it is not necessary to map the variables after the remeshing scheme. Additionally, the equidistant surface mesh is provided as an input to Mesh2D and remains unmodified. Therefore, the surface variables do not need to be mapped either.

Bibliography

Alberts, B., Johnson, A., Lewis, J., Morgan, D., Raff, M., Roberts, K., and Walter, P. (2015). The Cytoskeleton. In *Molecular Biology of the Cell*, chapter 16, pages 880–962. Garland Science, 6 edition.

Alhazmi, M. (2019). Exploring Mechanisms for Pattern Formation through Coupled Bulk-Surface PDEs in Case of Non-linear Reactions. *International Journal of Advanced Computer Science and Applications*, 10(3):556–568.

Allard, J. and Mogilner, A. (2013). Traveling waves in actin dynamics and cell motility. *Current Opinion in Cell Biology*, 25(1):107–115.

Alt, W. and Tranquillo, R. T. (1995). Basic morphogenetic system modeling shape changes of migrating cells, how to explain fluctuating lamellipodial dynamics. *Journal of Biological Systems*, 3(4):905–916.

Baaijens, F. P., Trickey, W. R., Laursen, T. A., and Guilak, F. (2005). Large deformation finite element analysis of micropipette aspiration to determine the mechanical properties of the chondrocyte. *Annals of Biomedical Engineering*, 33(4):494–501.

Barreira, R., Elliott, C. M., and Madzvamuse, A. (2011). Mathematical Biology The surface finite element method for pattern formation on evolving biological surfaces. *J Math Biol*, 63:1095–1119.

Barrett, J. W., Garcke, H., and Nürnberg, R. (2020). Chapter 4 - Parametric finite element approximations of curvature-driven interface evolutions. In Bonito, A. and Nochetto, R. H. B. T. H. o. N. A., editors, *Geometric Partial Differential Equations - Part I*, volume 21, pages 275–423. Elsevier.

Bhattacharya, S. and Iglesias, P. A. (2016). The Regulation of Cell Motility Through an Excitable Network. *IFAC PapersOnLine*, 49(26):357–363.

Brezzi, F., Falk, R. S., and Donatella Marini, L. (2014). Basic principles of mixed Virtual Element Methods. *ESAIM: Mathematical Modelling and Numerical Analysis*, 48(4):1227–1240.

Calderwood, D. A., Campbell, I. D., and Critchley, D. R. (2013). Talins and kindlins: Partners in integrin-mediated adhesion. *Nature Reviews Molecular Cell Biology*, 14(8):503–517.

Camley, B. A., Zhao, Y., Li, B., Levine, H., and Rappel, W. J. (2017). Crawling and turning in a minimal reaction-diffusion cell motility model: Coupling cell shape and biochemistry. *Physical Review E*, 95(1):1–13.

Campbell, E. J., Bagchi, P., Campbell, E. J., and Bagchi, P. (2017). A computational model of amoeboid cell swimming A computational model of amoeboid cell swimming. *Physics of Fluids*, 29:101902:1–101902:16.

Chang, C. M. E., D, D. A. L. P., and D, T. I. M. P. (2003). Motile chondrocytes from newborn calf : migration properties and synthesis of collagen II. *Osteoarthritis and Cartilage*, 11:603–612.

Cheng, B., Lin, M., Huang, G., Li, Y., Ji, B., Genin, G. M., Deshpande, V. S., Lu, T. J., and Xu, F. (2017). Cellular mechanosensing of the biophysical microenvironment: A review of mathematical models of biophysical regulation of cell responses. *Physics of Life Reviews*, 22-23:88–119.

Cheng, Y. and Othmer, H. (2016). A Model for Direction Sensing in Dictyostelium discoideum: Ras Activity and Symmetry Breaking Driven by a G$\beta\gamma$-Mediated, Gα2-Ric8 – Dependent Signal Transduction Network. *PLoS Computational Biology*, 12(5):e1004900.

Cooper, G. M. (2000). Structure and Organization of Actin Filaments. In *The Cell: A Molecular Approach*. Sunderland (MA): Sinauer Associates, 2 edition.

Cotton, M. and Claing, A. (2009). G protein-coupled receptors stimulation and the control of cell migration. *Cellular Signalling*, 21(7):1045–1053.

Cusseddu, D., Edelstein-Keshet, L., Mackenzie, J. A., Portet, S., and Madzvamuse, A. (2019). A coupled bulk-surface model for cell polarisation. *Journal of Theoretical Biology*, 481:119–135.

Da Yang, T., Park, J. S., Choi, Y., Choi, W., Ko, T. W., and Lee, K. J. (2011). Zigzag turning preference of freely crawling cells. *PLoS ONE*, 6(6):e20255.

de Boor, C. (1973). Good approximation by splines with variable knot. In *Numerical Solution of Differential Equations*, pages 12–20, Dundee. Lecture Notes in Math. 363, Springer, 1974.

Devreotes, P. and Horwitz, A. R. (2015). Signaling Networks that Regulate Cell Migration. *Cold Spring Harbor Perspectives in Biology*, 7(8):a005959.

Durand, R., Pantoja-rosero, B. G., and Oliveira, V. (2019). A general mesh smoothing method for finite elements. *Finite Elements in Analysis & Design*, 158(February):17–30.

Dziuk, G. and Elliott, C. M. (2007). Finite elements on evolving surfaces. *IMA Journal of Numerical Analysis*, 27(2):262–292.

Dziuk, G. and Elliott, C. M. (2013). Finite element methods for surface PDEs. *Acta Numerica*, 22(April):289–396.

Elliott, C. M. and Ranner, T. (2013). Finite element analysis for a coupled bulk-surface partial differential equation. *IMA Journal of Numerical Analysis*, 33(2):377–402.

Elliott, C. M., Ranner, T., and Venkataraman, C. (2017). Coupled Bulk-Surface Free Boundary Problems Arising from a Mathematical Model of Receptor-Ligand Dynamics. *SIAM Journal on Mathematical Analysis*, 49(1):360–397.

Elliott, C. M., Stinner, B., and Venkataraman, C. (2012). Modelling cell motility and chemotaxis with evolving surface finite elements. *J. R. Soc. Interface*, 9(June):3027–3044.

Elliott, C. M. and Styles, V. (2012). An ALE ESFEM for solving PDEs on evolvoing surfaces. *Milan J. Math.*, 80:469–501.

Engwirda, D. (2005). Unstructured mesh methods for the Navier-Stokes equations.

Engwirda, D. (2014). *Locally-optimal Delaunay-refinement and optimisation-based mesh generation.* PhD thesis, The University of Sydney.

Friedl, P. and Alexander, S. (2011). Cancer invasion and the microenvironment: Plasticity and reciprocity. *Cell*, 147(5):992–1009.

Frittelli, M., Madzvamuse, A., and Sgura, I. (2021). Bulk-surface virtual element method for systems of PDEs in two-space dimensions. *Numerische Mathematik*, 147(2):305–348.

Frittelli, M., Madzvamuse, A., Sgura, I., and Venkataraman, C. (2018). Numerical Preservation of Velocity Induced Invariant Regions for Reaction – Diffusion Systems on Evolving Surfaces. *J Sci Comput*, 77(2):971–1000.

Fuhrmann, J., Käs, J., and Stevens, A. (2007). Initiation of cytoskeletal asymmetry for cell polarization and movement. *Journal of Theoretical Biology*, 249:278–288.

Garzón-Alvarado, D. A., Galeano, C., and Mantilla, J. (2012). Numerical tests on pattern formation in 2d heterogeneous mediums : An approach using the schnakenberg model. *Dyna*, 172:56–66.

Gau, D. and Roy, P. (2020). Single Cell Migration Assay Using Human Breast Cancer MDA-MB-231 Cell Line. *Bio-protocol*, 10(8):e3586.

George, U. Z., Stéphanou, A., and Madzvamuse, A. (2013). Mathematical modelling and numerical simulations of actin dynamics in the eukaryotic cell. *Journal of Mathematical Biology*, 66(3):547–593.

Gierer, A. and Meinhardt, H. (1972). A theory of biological pattern formation. *Kybernetik*, 12(1):30–39.

Goehring, N. W. and Grill, S. W. (2013). Cell polarity : mechanochemical patterning. *Trends in Cell Biology*, 23(2):72–80.

Harris, P. J. (2017). A simple mathematical model of cell clustering by chemotaxis. *Mathematical Biosciences*, 294(May):62–70.

Heine, C. J. (2004). Isoparametric finite element approximation of curvature on hypersurfaces.

Holmes, W. R., Park, J., Levchenko, A., and Edelstein-keshet, L. (2017). A mathematical model coupling polarity signaling to cell adhesion explains diverse cell migration patterns. *PLoS Comput Biol*, 13(5):1–22.

Jarrell, K. F. and McBride, M. J. (2008). The surprisingly diverse ways that prokaryotes move. *Nature Reviews Microbiology*, 6(6):466–476.

Jeong, H. J., Yoo, R. J., Kim, J. K., Kim, M. H., Park, S. H., Kim, H., Lim, J. W., Do, S. H., Lee, K. C., Lee, Y. J., and Kim, D. W. (2019). Macrophage cell tracking PET imaging using mesoporous silica nanoparticles via in vivo bioorthogonal F-18 labeling. *Biomaterials*, 199(January):32–39.

Jung, H. J., Park, J. Y., Jeon, H. S., and Kwon, T. H. (2011). Aquaporin-5: A marker protein for proliferation and migration of human breast cancer cells. *PLoS ONE*, 6(12).

Krause, M. and Gautreau, A. (2014). Steering cell migration: lamellipodium dynamics and the regulation of directional persistence. *Nature Reviews Molecular Cell Biology*, 15(9):577–590.

Lehtimäki, J., Hakala, M., and Lappalainen, P. (2016). Actin Filament Structures in Migrating Cells. In Jockush, B. M., editor, *The Actin Cytoskeleton. Handbook of Experimental Pharmacology, vol. 235*, pages 123–152. Springer, Cham.

Lodish, H., Berk, A., Kaiser, C. A., Krieger, M., Bretscher, A., Ploegh, H., Amon, A., and Scott, M. P. (2016). Organización y Movimiento Celular I: Microfilamentos. In *Biología Celular y Molecular*, chapter 17, pages 773–820. Editorial Médica Panamericana, 7 edition.

Luxenburg, C. and Zaidel-bar, R. (2019). From cell shape to cell fate via the cytoskeleton — Insights from the epidermis. *Experimental Cell Research*, 378(2):232–237.

Mackenzie, J. A., Nolan, M., Rowlatt, C. F., and Insall, R. H. (2019). An Adaptive Moving Mesh Method for Forced Curve Shortening Flow. *SIAM J. Sci. Comput.*, 41(2):1170–1200.

Madzvamuse, A. and George, U. Z. (2013). The moving grid finite element method applied to cell movement and deformation. *Finite Elements in Analysis and Design*, 74:76–92.

Madzvamuse, A., Maini, P. K., and Wathen, A. J. (2005). A moving grid finite element method for the simulation of pattern generation by turing models on growing domains. *Journal of Scientific Computing*, 24(2):247–262.

Meinhardt, H. (1999). Orientation of chemotactic cells and growth cones : models and mechanisms. *Journal of Cell Science*, 112:2867–2874.

Morales, T. (2007). Chondrocyte Moves : clever strategies ? *Osteoarthritis Cartilage*, 15(8):861–871.

Mori, Y., Jilkine, A., and Edelstein-Keshet, L. (2008). Wave-pinning and cell polarity from a bistable reaction-diffusion system. *Biophysical Journal*, 94(9):3684–3697.

Murray, J. D. (2002). *Mathematical Biology : I . An Introduction*. Springer, 3 edition.

Murray, J. D. (2003). *Mathematical Biology II : Spatial Models and Biomedical Applications*. Springer, 3 edition.

Neilson, M. P., Mackenzie, J. A., Webb, S. D., and Insall, R. H. (2011). Modeling cell movement and chemotaxis using pseudopod-based feedback. *Computational Methods in Science and Engineering*, 33(1):1035–1057.

Novak, I. L., Gao, F., Choi, Y.-S., Resasco, D., Schaff, J. C., and Slepchenko, B. M. (2007). Diffusion on a curved surface coupled to diffusion in the volume: Application to cell biology. *Journal of Computational Physics*, 226(2):1271–1290.

Ojima, Y., Hakamada, K., Nishinoue, Y., Nguyen, M. H., Miyake, J., and Taya, M. (2012). Motility behavior of rpoS -deficient Escherichia coli analyzed by individual cell tracking. *Journal of Bioscience and Bioengineering*, 114(6):652–656.

Othmer, H. G. (2019). Eukaryotic cell dynamics from crawlers to swimmers. *Wiley Interdisciplinary Reviews: Computational Molecular Science*, 9(1):e1376.

Page, K., Maini, P. K., and Monk, N. A. M. (2003). Pattern formation in spatially heterogeneous Turing reaction – diffusion models. *Physica D*, 181:80–101.

Page, K. M., Maini, P. K., and Monk, N. A. M. (2005). Complex pattern formation in reaction–diffusion systems with spatially varying parameters. *Physica D*, 202:95–115.

Piltti, K. M., Cummings, B. J., Carta, K., Manughian-peter, A., Worne, C. L., Singh, K., Ong, D., Maksymyuk, Y., Khine, M., and Anderson, A. J. (2018). Live-cell time-lapse imaging and single-cell tracking of in vitro cultured neural stem cells – Tools for analyzing dynamics of cell cycle , migration , and lineage selection. *Methods*, 133:81–90.

Preziosi, L. and Tosin, A. (2009). Multiphase modelling of tumour growth and extracellular matrix interaction: Mathematical tools and applications. *Journal of Mathematical Biology*, 58(4-5):625–656.

Rätz, A. (2015). Turing-type instabilities in bulk–surface reaction–diffusion systems. *Journal of Computational and Applied Mathematics*, 289:142–152.

Rätz, A. and Röger, M. (2014). Symmetry breaking in a bulk–surface reaction–diffusion model for signalling networks. *Nonlinearity*, 27(8):1805–1827.

Ridley, A. J. (2015). Rho GTPase signalling in cell migration. *Current Opinion in Cell Biology*, 36:103–112.

Ridley, A. J., Schwartz, M. A., Burridge, K., Firtel, R. A., Ginsberg, M. H., Borisy, G., Parsons, J. T., and Horwitz, A. R. (2003). Cell Migration: Integrating Signals from Front to Back. *Science*, 302(5651):1704–1709.

Rodrigues, D., Barra, L. P., Lobosco, M., and Bastos, F. (2014). Analysis of Turing Instability in Biological Models. In *ICCSA, Part VI*, pages 576–591.

Salloum, G., Jaafar, L., and El-Sibai, M. (2020). Rho A and Rac1: Antagonists moving forward. *Tissue and Cell*, 65(March):101364.

Schnakenberg, J. (1979). Simple Chemical Reaction Systems with Limit Cycle Behaviour. *J Theor Biol*, 81:389–400.

Séguis, J.-C., Burrage, K., Erban, R., and Kay, D. (2012). Simulation of cell movement through evolving environment : a fictitious domain approach. Technical report, University of Oxford.

Sel'kov, E. E. (1968). Self-Oscillations in Glycolysis. *European Journal of Biochemistry*, 4(1):79–86.

Seydel, R. (2010). *Practical Bifurcation and Stability Analysis*. Springer, 3 edition.

Shah, E. A. and Keren, K. (2013). Mechanical forces and feedbacks in cell motility. *Current Opinion in Cell Biology*, 25(5):550–557.

Steffen, A., Stradal, T. E. B., and Rottner, K. (2016). Signalling Pathways Controlling Cellular Actin Organization. In Jockush, B. M., editor, *The Actin Cytoskeleton. Handbook of Experimental Pharmacology, vol. 235*, pages 153–178. Springer, Cham.

Stéphanou, A. and Tracqui, P. (2002). Cytomechanics of cell deformations and migration : from models to experiments. *C. R. Biologies*, 325:295–308.

Ting, L. H., Jahn, J. R., Jung, J. I., Shuman, B. R., Feghhi, S., Han, S. J., Rodriguez, M. L., and Sniadecki, N. J. (2012). Flow mechanotransduction regulates traction forces , intercellular forces , and adherens junctions Flow mechanotransduction regulates traction forces , intercellular forces , and adherens junctions. *Am J Physiol Heart Circ Physiol*, 302(March):2220–2229.

Turing, A. M. (1952). The Chemical Basis of Morphogenesis. *Philosophical transactions of the Royal Society of London. Series B, Biological sciences*, 237(641):37–72.

Uriu, K., Morelli, L. G., and Oates, A. C. (2014). Interplay between intercellular signaling and cell movement in development. *Seminars in Cell and Developmental Biology*, 35:66–72.

Vu, H., Zhou, J., Huang, Y., Hakamivala, A., and Kyung, M. (2019). Development of a dual-wavelength fluorescent nanoprobe for in vivo and in vitro cell tracking consecutively. *Bioorganic & Medicinal Chemistry*, 27(9):1855–1862.

Warner, H., Wilson, B. J., and Caswell, P. T. (2019). Control of adhesion and protrusion in cell migration by Rho GTPases. *Current Opinion in Cell Biology*, 56:64–70.

Welf, E. S. and Haugh, J. M. (2011). Signaling pathways that control cell migration: models and analysis. *Wiley Interdisciplinary Reviews: Systems Biology and Medicine*, 3(2):231–240.

Zhao, J., Cao, Y., Dipietro, L. A., and Liang, J. (2017). Dynamic cellular finite-element method for modelling large-scale cell migration and proliferation under the control of mechanical and biochemical cues : a study of re-epithelialization. *J. R. Soc. Interface*, 14(129).